CFD Analysis of Coal and Heavy Oil Gasification for Syngas Production

Sreedharan, Vikram

Publication date:
2012

Document Version
Early version, also known as pre-print

1. INTRODUCTION

Gasification is often defined as the conversion of any carbon containing fuel to a gaseous product with some useful heating value. Processes such as hydrogenation, pyrolysis and partial oxidation are covered by this definition whereas, combustion is not. This is because the flue gases produced during combustion do not have any residual heating value.

1.1 Historical Perspective

In the past (especially the 18^{th} and 19^{th} centuries), pyrolysis was a gasification technology that was commonplace. However, partial oxidation had almost completely supplanted pyrolysis from the 1930s onward. A process involving pyrolysis of coal to produce gas was first developed mainly for industrial applications, in the 18^{th} century. The production of coke using coke ovens, and its use as a substitute for charcoal in the metallurgical industry was a precursor to coal pyrolysis. The use of coke ovens were necessitated by massive deforestation and the resulting consumption of wood (as charcoal) for production of iron in 17^{th} century England. The first large-scale utilization of pyrolysis was by the London Gas, Light and Coke Company (founded in 1812) to produce "town gas", which became the most widely used gaseous fuel in the first half of the industrial era (Higman and van der Burgt, 2008). Pyrolysis and the water-gas process were used to produce the town gas. The pyrolysis of coke

obtained from discontinuously operating ovens produced town gas with a relatively high heating value (20 - 23MJ/m^3), whereas the water-gas process was used to convert coke into a mixture of carbon dioxide and hydrogen of a lower heating value (about 12MJ/m^3).

Illumination and cooking were the early domestic applications for town gas due to gasification being an expensive process in the 19th century. Electric bulbs then began to slowly replace town gas for illumination purposes by about 1900. Later in the 20th century, increased prosperity led to a return of gas for space heating in homes. First with coal and then town gas, followed by a brief tryst with heating oil, domestic space heating became more prevalent with the use of natural gas. The earlier experience with town gas was instrumental in assuaging fears of potential gas explosions with the use of natural gas. More recent developments have led to industrial gas being used not just for heating, but also as a raw material for the chemical industry as well as for electrical power production. Long-distance transportation of town gas in an economical manner was difficult due to its low heating content. The development of materials and manufacturing methods for tubes, drums, pipes and pressure/reactor vessels made possible the advent of steam locomotion technology, gasification and different chemical industries. Prior to the maturation of this technology, it was a problem to produce gas-tight equipment that could store gases at pressures in excess of 2bar. This is one of the main reasons for the comparatively large size and bulk of early transportation and storage vessels.

Development of a continuous gasification process using an oxygen blast was made possible by commercialization of the cryogenic separation of air in the 1920s by Carl von Linde. This significant advance was followed by others such

as the Winkler fluid-bed process (1926), Lurgi moving-bed process (1931) and the Koppers-Totzek entrained-flow process (1940s). With the commercialization and widespread deployment of these technologies, not much additional technological progress was achieved with regards to the gasification of solid fuels for the next 40 years or so. However, in utilizing these technologies, capacity was steadily increased in order to produce synthetic fuels. South African Coal, Oil and Gas Corporation, known as SASOL in more recent years was also started up in the same period. This company developed a synfuels complex and an extensive petrochemicals industry through coal gasification and the Fisher-Tropsch process. By the 1970s, the extended SASOL complex was the largest gasification center in the world.

A shift in the relative importance of coal gasification was brought about in the 1950s by discoveries of abundant quantities of naphtha and natural gas. The demand for synthesis gas increased around the same period as well, due to the exponential demand growth for ammonia as a nitrogenous fertilizer. Large-scale steam-reforming of natural gas and naphtha was considered necessary to meet this growing demand. The 1950s was also the period when both the Texaco (currently, GE) and Shell Oil Gasification processes were developed. Though nowhere near as widely used as steam reforming for production of ammonia for the fertilizer industry, these technologies were able to satisfy demand in places with a shortage of naphtha and natural gas. Renewed interest in coal gasification was brought about by a perceived shortage in natural gas during the first oil crisis in the early 1970s, due to the technology's potential for the production of liquid and gaseous fuels. Much of the revival efforts were focused on coal hydrogenation for the so-called "hydro-gasification" and direct

liquefaction technologies. The former was aimed at hydrogenating coal directly to methane, to be used as a substitute natural gas (SNG). Despite some significant developments, what inhibited full commercialization were the high costs associated with high-pressure operation as dictated by process thermodynamics. Interest in fuels technology has also led to further development in older processes (Higman and van der Burgt, 2nd Ed., 2008). Lurgi in collaboration with British Gas (BGL) built on its existing technology to develop a slagging version of its original moving-bed design. A pressurized version of the Koppers-Totzek gasifier was developed by Shell with technical inputs from Koppers (the Koppers version is sold as Prenflo and Shell's as its own Coal Gasification Process). Texaco extended its own oil gasification technology to accept slurry feed coal, and Rheinbraun developed the High-Temperature Winkler (HTW) fluidized-bed process.

Due to current concerns about global environmental conditions, in response to recent shifts in feedstock price fluctuations (for example, natural gas), national energy security concerns and safety concerns, gasification technologies are again gaining recognition worldwide. This recognition is primarily in the requirement of power, particularly Integrated Gasification Combined Cycle (IGCC) technology. Gasification is also of interest in developing energy saving technologies and high-efficiency technologies of unused resources and wastes for a human recycling-oriented society (Hasegawa, 2007).

1.2 Argument for Gasification

Some examples of non-power related installations of gasifiers include (Jenkins, GTC Workshop, 2008),

a) The "coals-to-chemicals" facility operated by Eastman Chemicals in Kingsport, Tennessee since 1983. This plant used Texaco (GE Energy) gasifiers with a feed of 1300tons of central Appalachian medium sulfur coal per day. With the removal of sulfur compounds and ash, the resultant syngas was used to produce methanol, acetic acid, acetic anhydride, methyl acetate and various consumer products.
b) The Great Plains synfuel plant operated by the Dakota Gasification Company. This facility was started up in 1984 in Beulah, North Dakota as part of the Basin Electric Power cooperative. This plant converts 16000tons/day of North Dakota lignite to synthetic natural gas (SNG), fertilizers and chemicals.
c) The Coffeyville Resources Coal to Fertilizer plant in Kansas. Earlier, this plant utilized high-cost natural gas to make hydrogen for ammonia. The subsequent addition of a petcoke gasification system using a GE Energy (Texaco) gasifier made possible syngas production with high hydrogen content. This hydrogen was used to synthesize ammonia, resulting in significant production cost savings and improved profitability.

Proposed gasification plants for production of ammonia, Fischer-Tropsch fuels (diesel and naphtha), hydrogen, methanol, methyl acetate, SNG, urea and urea ammonium nitrate use feedstock as diverse as coal, petcoke,

refinery waste streams, biomass and blends of the aforementioned feeds. The other significant utilization of gasification is to produce syngas to drive gas turbines in integrated gasification combined cycle (IGCC) power plants.

1.3 Gasification or Combustion

The primary difference is the mix of product gases obtained during gasification or combustion. They are summarized in Table 1.1:

Element	Gasification	Combustion
Carbon	CO	CO_2
Hydrogen	H_2	H_2O
Nitrogen	HCN, NH_3 or N_2	NO and NO_2
Sulfur	H_2S or COS	SO_2 or SO_3

Table 1.1: Difference between gasification and combustion products

Unlike combustion where the primary products are CO_2 and H_2O (with traces of NO_x and SO_x), with gasification, a mixture of CO and H_2 is obtained with traces of HCN, NH_3 or N_2, and H_2S or COS. Another difference between the two processes is the amount of heat that is released by the chemical reactions. In combustion, all of the feedstock's chemical energy is converted and released as heat energy (complete conversion assumed), whereas most of the feed's chemical energy remains in the product syngas as its heating value in

gasification (Jeffrey Phillips, The Gas Turbine Handbook, 2006). Since the amount of heat released during gasification is far lower, it is important to limit the transport of heat energy from the gasification "zone", else; the temperature within this zone might fall below the threshold temperature at which the gasification reactions can self-sustain (minimum of about 1300K). Gasifiers also typically operate at high pressures (upto 7MPa), which permits compact design with a small surface area and minimal heat loss.

1.4 Classification of Gasifiers

Gasifiers can be grouped into the following classes based on flow geometry:

1.4.1 Fixed-Bed

This is the simplest and oldest type of gasifier. These gasifiers are based on technologies developed in the 1800s and early 1900s, and are currently not as popular as entrained-flow gasifiers for applications such as power generation. These gasifiers have a large residence time, and are less capital intensive with fuel flexibility being a significant advantage. Many of the fixed-bed gasifiers developed in the early 1900s were of small-scale, processing less than 100 tons of coal or coke per day, and used air and steam as reactants. During the oil crisis of the 1970s, industries were encouraged to build small gasifiers to generate low heating value gas as a natural gas replacement for their processes (PERI Report for US DOE, 2003). Most existing fixed-bed gasification

technologies are based on these earlier developments with additional modifications and improvements.

In these gasifiers, gases flow relatively slowly upward through a coal bed. The only industrial-scale gasifiers currently in use which utilize fixed bed technology are – British Gas-Lurgi (BGL), Lurgi dry ash and Bharat Heavy Electricals Limited (BHEL). BGL is a slagging type gasifier, while Lurgi and BHEL are dry ash gasifiers. These gasifiers are only suitable for solid fuels, and the BGL gasifier is the only one that operates at temperatures well in excess of 1000ºC. The BHEL and Lurgi gasifiers are more suited to reactive coal feeds such as lignite. To prevent problems such as unstable outlet gas temperatures and composition, or worse, downstream explosions, pressure drops need to be avoided by incorporating good bed permeability in these gasifiers. In older designs, caking was an undesirable property to be avoided, due to the inability to process melting particles which sintered together to form larger agglomerated clumps when heated. In the Lurgi dry ash gasifier, caking coals can be processed only when they are blended with non-caking coals. The tolerance for coal fines (powder) varies between 5% in the Lurgi dry ash gasifier to almost 50% in the case of the BGL gasifier.

The main characteristics of this gasifier type can be summarized as follows (Jeffrey Phillips, The Gas Turbine Handbook, 2006):

a) Limited ability to handle fines.
b) Special requirements for handling caking coal.
c) Relatively high methane content in the product gas.
d) Low oxidant requirements.

e) High “cold gas” thermal efficiency when the heating values of the product hydrocarbon liquids are included.
f) Hydrocarbon liquids such as tars and oils form part of the product stream.

1.4.2 Fluidized-Bed

These air or oxygen-blown gasifiers typically operate with solid crushed fuels (0.5 – 5mm), which can be either of the bubbling or the circulating-bed type. Solid fuel particles are suspended in an upward flow of gas, and hence are fluidized. A typical bed is formed from char, sorbent, ash and sand. The residence time of the fuel particles vary between 10 seconds and about 2 minutes. Fluidized beds operate well below the ash fusion temperature for the solid feed to prevent the ash contained in it from melting (Collot, IEA Clean Coal Centre Profiles, 2002). For this reason, strict control of gasifier operating temperatures is required while processing solid feeds (such as coal) with high alkali content. In other words, the range of operating temperatures of this gasifier type is less than that of entrained-flow gasifiers. Typical operating temperatures and pressures are 1000 – 1400K and 0.1 – 3MPa, respectively. Usually, oxygen-blown gasifiers are preferred since they yield a product gas with higher heating value than an air-blown gasifier.

A drawback of this gasifier type in comparison with an entrained-flow type gasifier is the lower rate of carbon conversion attributable to the lower operating temperatures. An improvement in carbon conversion can be brought about by either reburning char in a separate combustion unit, or by recirculating

the char to the gasifier. The lower operating temperature of this gasifier type also means avoidance of expenditure on a high-temperature gas cooling system. Fluidized-beds may also be sub-classified based on the ash-discharge method; the use of dry or agglomerated ash removal systems. Say for instance, with a solid feed like coal if agglomeration is an undesirable trait then, a coal with a low swelling index (low caking) is preferred. The ability to handle agglomerated ash makes it possible to use high-rank coals whereas dry ash removal systems offer high system turndown flexibility. Fluidized-bed gasifiers are also more tolerant to feeds with high sulfur content, since sorbents in the bed help retain sulfur (by as much as 90%). There are six types of commercial gasification processes using fluidized-beds (PERI Report for US DOE, 2003): Integrated Drying Gasification Combined Cycle (IDGCC), High Temperature Winkler (HTW), Kellogg Rust Westinghouse (KRW), Bharat Heavy Electricals Limited/Indian Institute of Technology (BHEL/IIT), Air Blown Gasification Cycle (ABGC) and Transport Reactor Gasifier (TRG).

In the 1980s and 1990s, fluidized-bed gasifiers were operated commercially primarily for the synthesis of chemicals and to demonstrate their fitness for use in IGCC plants for power generation. One promising new venture is the development of a fluidized-bed partial gasification process by Foster Wheeler, in collaboration with the US Department of Energy (DOE); technology which could potentially turn out to be more cost-effective than that used currently for IGCC. New fluidized-bed plants based on the High Temperature Winkler (HTW) process are also under trial in the Czech Republic. Small-scale plants in China (U-Gas) utilizing Gas Technology Institute's (GTI) "know how" are currently producing syngas as feedstock for chemical synthesis. Steam-

reforming technology is also being used as a focal point for small-scale plants in Canada and the US, with these facilities using black liquor or biomass as feed.

Fluidized-bed gasifiers are characterized by:

a) Uniform and moderate temperatures, lower than that for entrained-flow gasifiers.
b) Moderate oxygen and steam requirements.
c) Extensive solids recycling required for high carbon conversion.

1.4.3 Entrained-Flow

Currently, entrained-flow gasification is the most widely used large-scale gasification process in the world for power generation. In this gasifier type, pulverized solid feed (such as coal), biomass pellets or oil droplets and gases flow concurrently at high speed. Short gas residence times require the solid feed to be pulverized into small granules or reconstituted into pellets (for biomass) to ensure high carbon conversion. These gasifiers can accept and utilize both solid and liquid fuels. There are seven different entrained-flow gasification technologies currently in commercial operation, namely – Hitachi, E-Gas, Babcock Borsig Power (BBP), Shell Coal Gasification Process (SCGP), Texaco (now GE), Mitsubishi Heavy Industries (MHI) and Prenflo.

Entrained-flow gasifiers operate at high temperatures, 1250 – 2200K and pressures, 2 – 8MPa. High carbon conversion is ensured by the high operating temperature, which generally exceeds the ash fusion temperature to produce

relatively high heating value syngas free from liquid hydrocarbons. For gasifiers designed with walls which require a slag-coating to function optimally by minimizing heat loss through the wall, there is a minimum ash content requirement. A maximum ash content requirement also needs to be fixed depending on the type of entrained-flow gasifier technology used (Collot, IEA Clean Coal Centre Profiles, 2002). The optimum ash fusion temperature of the feed should be less than the operating temperature of the gasifier (1650 – 1900K). For slags that exhibit crystalline behavior, critical temperature viscosity is another important factor that is influenced by slag composition (SiO_2/Al_2O_3). In order for a particular gasifier design to operate on a number of feeds, either the feed is blended with a flux or with a feed having a low ash fusion temperature.

Some identifying characteristics of entrained-flow gasifiers are:

a) Different kinds of liquid and solid fuels including coal of all ranks, caking characteristics and amount of fines.
b) Requirement of a large amount of oxidant.
c) Raw syngas with a large amount of sensible heat.
d) High-temperature slagging operation.
e) Molten slag being entrained by the raw syngas.

1.4.4 Hybrid and Novel

In addition to the main three types of gasifiers already discussed, there also exist gasifiers that are based on hybrid combinations of those flow geometries,

an example of which is the Kellogg Brown and Root (KBR) gasifier. This is a hybrid gasifier since it has the characteristics of both an entrained-flow and a fluidized-bed gasifier. An example of a novel gasifier would be a molten metal bath gasifier.

1.5 State-of-the-Art

The methods used to model the physical and chemical processes within a gasifier will vary depending on the particle/droplet loading (by volume fraction) in the gasifier, hence it will be different for different gasifier types. For a fluidized bed reactor, a multiphase flow model known as the two fluid model (TFM) using an Euler-Euler approach may have to be used to account for particle-particle interactions for a flow which is dense, that is, if the particle volume fraction is much greater than 10%. There is also the possibility of incorporating a coefficient of restitution for particle collisions occurring within the reactor (Du et al, 2006). The TFM technique can be implemented using FLUENT. Euler-Euler models have also been developed for entrained-flow gasifiers (Vicente et al, 2003), and TFM can be modified to accommodate a multi fluid model or MFM (Gera et al, 2004). Considering a novel type of gasifier such as a molten bath gasifier, the foamy molten slag (continuous phase) can be modeled as a single-phase fluid using an Eulerian approach, while the bubbles (discrete phase) can be tracked within the reactor using a Lagrangian approach (Skodras et al, 2003).

For the present study, the processes of interest occurring within an entrained-flow gasifier are studied using computational fluid dynamics models utilizing an Euler-Lagrange description. Hence, all future discussions will be restricted to gasifiers of the entrained-flow type.

An excellent overview of the CFD models developed between 1970 and 1980 for combustion and gasification of pulverized coal is presented by Smoot (1984). Most of these early models are one- or two-dimensional steady-state formulations incorporating devolatilization, heterogeneous reactions and gas-phase reactions. Wen and Chaung (1978) developed a single-step pyrolysis model with rate expressions for the reaction of char with CO_2, O_2 and H_2 and a global rate for gaseous equilibrium. A similar model was used by Govind and Shah (1984) to compare their results with experimental data from a Texaco entrained-bed pilot-plant gasifier for different feeds (coal liquefaction residue and coal water slurry). Some of the more advanced models, Lockwood et al (1980) for instance, also include Lagrangian particle motion, a k-ε turbulence model and radiation modeling.

Bockelie et al (2002) used local mixing calculations to determine gas properties, with the assumption of random fluctuations following a statistical probability density function (PDF) which is a characteristic of turbulent flows. A flowing slag sub-model was also included in that model. More comprehensive sub-models for slag have been developed by Wang et al (2007) and others.

Choi et al (2001) considered different injection velocities as well as oxygen inlet diameter, injection angles and burner length in their study. They used an

unreacted-core shrinking model for the char (heterogeneous) reactions and a modified eddy break-up (EBU) for the gas-phase (homogeneous) reactions. Chui et al (2009) compared the effect of coal devolatilization and char reactions occurring simultaneously versus char reactions being delayed till devolatilization is completed. They discovered that in the latter case, the char reaction zone was pushed further away from the burner, but this zone did not extend much further along the reactor length when compared to the former. Wu et al (2009) estimated the characteristic time and length scales for major processes within an entrained-flow coal gasifier. They used a chemical kinetics model for the gas-phase reactions based on a modified Arrhenius rate relation with most parameter values adopted from Jones and Lindstedt (1988) and Westbrook and Dryer (1981). They concluded that in the flame region, there is a strong coupling between macro-scale turbulent fluctuations and char (heterogeneous) reactions, while the Kolmogorov micro-scales influence the combustion of volatiles.

Silaen and Wang (2010) used FLUENT to compare the different turbulence models as applied to the gasifier in Chen et al (2000). They compared the standard k- ε, k-ω, RSM, k-ω SST and k- ε RNG models and concluded that the results obtained with the k- ε model are satisfactory, as are the results from the k-ω SST model and the higher-order RSM model.

Chen et al (2000) used a chemical kinetics model in which the heterogeneous reaction rates were described by Arrhenius relations and the gas-phase reactions were assumed to be limited by the mixing rate of the reactants and not by the reaction kinetics. On the other hand, Watanabe and Otaka (2006) used Arrhenius rate expressions for both the heterogeneous and gas phase reactions.

The effective reaction rate for the gas-phase reactions was determined as the minimum between the Arrhenius reaction rates and turbulent mixing rate from the eddy breakup model. Ajilkumar et al (2009) used the heterogeneous reaction rates from Chen et al (2000) and the gas-phase reaction rate parameters from Watanabe and Otaka (2006) for modeling a steam-assisted tubular coal gasifier.

Niksa et al (2003) provides a good overview of experimental work to determine devolatilization and char oxidation mechanisms and development of coal conversion sub-models. Soelberg et al (1985) and Brown et al (1988) conducted experiments to determine species distributions for carbon, monoxide, hydrogen and carbon dioxide for different locations within an entrained-flow lab-scale coal gasifier, thus estimating their spatial distribution. Smoot and Brown (1987) investigated the controlling mechanisms for the gasification of pulverized coal at atmospheric pressure. This work forms a suitable basis for the kinetic reaction rate parameters for different kind of coals as well the parameters required for the Kobayashi model.

Watanabe et al (2002) developed a CFD model for the gasification of Orimulsion^{TM} as an evaluation tool for the performance of an extra heavy oil gasifier and for refinement of its design. In this model they considered both the heterogeneous char reactions (with steam, carbon dioxide and water vapour) as well as gas-phase reactions. Vaezi et al (2011), also developed a numerical model for gasification of the same feed based on the experimental results of Ashizawa et al (2005). This study did not consider heterogeneous char reactions.

Traditionally, the simplified global reaction schemes proposed by Westbrook and Dryer (1981), Jones and Lindstedt (1988) and Goyal and Gidaspow (1982) have been used extensively in modeling gasification using computational fluid dynamics. However, with an increase in computational power and storage, more complex reaction schemes such as those proposed by Bradley et al (2001) and Alam et al (2010) are now practical. Proposals for a comprehensive reaction path scheme for pyrolysis and gasification of heavy oil, while also being computationally tractable have been proposed by Maki and Miura (1996) and more recently by Mailybaev et al (2011).

1.6 Motivation

The background for this work is the increased use of coal and heavy oil foreseen within Statoil both as energy carriers and in context of CO_2 management. A method to utilize coal and heavy oil is to gasify and oxidize the hydrocarbons in a reactor to produce synthesis gas.

The aim of this work is to analyze the different physical and chemical processes taking place within the reactor, develop computational fluid dynamics (CFD) models incorporating these processes, compare the CFD predictions with experimental data, and select the most appropriate model.

2. GASIFICATION MODELING

Gasification involves a number of complex physical and chemical processes such as turbulence, multiphase flow, heat transfer, mass transfer and chemical reactions. When a feedstock is introduced into the reactor at high temperature, usually with air or oxygen as a carrier, a number of physical and chemical processes occur within the gasifier. Quite often, to obtain the benefit of savings in space and energy, gasification takes place at high pressures with a suitable design of the reactor vessel. If the feedstock used is coal, for a dry feed the volatile portion in the coal particles is consumed during devolatilization and the resulting char is burned or gasified. If coal slurry is used as the feedstock, the moisture has to be evaporated from the coal particles before devolatilization can take place, and this leads to more energy being consumed for this type of feed. In the case of heavy oil, due to the high moisture content of bitumen emulsions such as Orimulsion^{TM}, a not inconsiderable amount of energy is expended to evaporate the moisture before the droplets are gasified and the resulting char consumed.

When these processes are occurring, simultaneously gaseous products from the gasification of coal particles or oil droplets will be ignited, or react with other species based on the surrounding environment and their intrinsic kinetics mechanisms (Choi et al, 2001). These reactions and processes cannot be modeled in their entirety due to the heterogeneity and complexity of coal or

heavy oil. Based on experiments and simplified mechanisms, this process can be divided further into several simple sub-processes.

In an entrained-flow gasifier, the coal particles would mainly follow the gas flow which is represented typically as a dilute flow regime. This assumption also holds true of heavy oil droplets till the volatile content is consumed. In this regime, the volume occupied by the particles and the particle-particle interaction are assumed to be negligible. A common criterion for dilute flow is that the particle mass fraction should be less than 10%.

The CFD modeling of gasification of different types of feedstock are all slightly different with the same basic principles underlying these processes. The two main aspects of gasification which need to be included in the CFD model are: 1. Multiphase Flow, and 2. Gasification.

The commercial CFD software ANSYS Fluent which has the ability to handle turbulent, reactive gas-particle flow has been used for the modeling work (Fluent, 2010).

2.1 Multiphase Flow

When the flow is dilute, a discrete phase model (DPM) is applicable to model the flow of both the continuous gas phase and the particles (or droplets). Using DPM, the particle trajectories are estimated along with mass and energy transfer to/from the particles using a Lagrange formulation (Shi et al, 2006). Hence an Euler-Lagrange description of the flow is necessary when the DPM technique is

used. The coupling between the continuous phase and the discrete phase is solved by tracking the exchange of mass, momentum and energy.

2.1.1 Continuous Phase

The continuous gas phase is characterized by Favre-averaged equations for fluid flow based on the laws of conservation of mass, momentum and energy as given in Versteeg & Malalasekara (2007). These governing transport equations can be written using Cartesian tensor notation in a generalized form given by

$$\frac{\partial}{\partial t}(\rho\Phi)+\frac{\partial}{\partial x_j}(\rho u_j\Phi)=\frac{\partial}{\partial x_j}\left(\Gamma_\Phi\frac{\partial\Phi}{\partial x_j}\right)+S_\Phi+S_{\Phi P} \qquad (2.1)$$

Here, the dependent parameter could represent any of the following variables, given by $\Phi=1,u_i,h,Y_k,k,\varepsilon,G$, that is, mass, momentum, energy (thermal), species, turbulent kinetic energy, turbulent energy dissipation rate and incident radiation. S_Φ is a standard source term in the governing equations (Versteeg & Malalasekara, 2007) and $S_{\Phi P}$ is the inter-phase source term (Fluent 2010), which takes into account the interaction of the continuous phase with the discrete particle phase.

Turbulence is described by the standard $k-\varepsilon$ turbulence model (Versteeg & Malalasekara, 2007), where the length and time scale of the large energy-containing eddies is determined from the turbulent kinetic energy and its dissipation rate. Turbulent Reynolds stresses are modeled by the Boussinesq hypothesis as

$$-\rho\overline{u_i'u_j'} = \mu_t\left(\frac{\partial u_i}{\partial x_j}+\frac{\partial u_j}{\partial x_i}\right)-\frac{2}{3}\left(\rho k+\mu_t\frac{\partial u_k}{\partial x_k}\right)\delta_{ij} \tag{2.2}$$

In a similar manner, turbulent Reynolds fluxes are modeled by the gradient diffusion hypothesis as

$$-\rho\overline{u_j'\phi'} = \frac{\mu_t}{\sigma_\Phi}\frac{\partial \Phi}{\partial x_j} \tag{2.3}$$

where σ_Φ is the turbulent Prandtl/Schmidt number for variable Φ. The turbulent eddy viscosity is given by

$$\mu_t = \rho C_\mu \frac{k^2}{\varepsilon} \tag{2.4}$$

Accordingly, the transport coefficient in the general transport equation (2.1) can be defined as

$$\Gamma_\Phi = \frac{\mu_t}{\sigma_\Phi} \tag{2.5}$$

The radiation is described by the P1 model which is the simplest of the P-N models (Siegel & Howell, 1992) based on the expansion of the radiation intensity into an orthogonal series of spherical harmonics. The P1 radiation model can include radiation from a secondary dispersed phase. Assuming gray radiation with isotropic scatter, the radiative flux can be expressed as

$$q_{rj} = -\frac{1}{3(a+\sigma_S)}\frac{\partial G}{\partial x_j} \tag{2.6}$$

where a is the absorption coefficient, and σ_S is the scattering coefficient. Accordingly, the transport coefficient in the general transport equation (2.1) can be defined as

$$\Gamma_\Phi = \frac{1}{3(a+\sigma_S)} \tag{2.7}$$

The effect of particles can also be included in the P-1 radiation model.

2.1.2 Discrete Phase

The mass conservation equation for the discrete phase (particles or droplets) takes the following form:

$$\frac{dm_p}{dt} = \sum_{i=1}^{N} \frac{dm_i}{dt} \tag{2.8}$$

The mass of the discrete phase is consumed by the *N* volatiles oxidation, char combustion and char gasification reactions taking place on the surface of the particle. The mass of gas produced by each of these heterogeneous reactions is denoted m_i.

The trajectory of a discrete-phase particle is determined from Newton's second law of motion. The force balance on the particle can be written:

$$\frac{du_{pi}}{dt} = F_D\left(u_{gi} - u_{pi}\right) + g_i \frac{\left(\rho_p - \rho_g\right)}{\rho_p} + \frac{\rho_g}{2\rho_p}\frac{d}{dt}\left(u_{gi} - u_{pi}\right) + \left(\frac{\rho_g}{\rho_p}\right) u_{pj}\frac{\partial u_{gi}}{\partial x_j} \tag{2.9}$$

Here, the particle inertia is balanced by the external drag, gravity, virtual mass and pressure forces acting on the particle. Typically, the contribution of virtual mass is almost negligible (less than 0.1% of the particle mass). For a rigid spherical particle the drag is defined by (Haberman & Sayre, 1958)

$$F_D = \frac{18\mu_g}{\rho_p d_p^2}\frac{\mathrm{Re}\, C_D}{24} \tag{2.10}$$

Turbulent dispersion of the particles due to turbulence in the continuous phase is included in the particle tracking. The instantaneous velocity of the continuous phase is expressed as

$$u_i = \overline{u_i} + u_i' \tag{2.11}$$

The fluctuation velocity is found from the turbulent kinetic energy as

$$u_i' = \zeta\sqrt{2k/3} \tag{2.12}$$

Where, ζ is a standard normally distributed random number, and $\zeta = 1$ for isotropic turbulence. The particle is assumed to interact with the continuous phase turbulence over a period of time, which is equal to the smaller of the eddy lifetime and the particle eddy crossing time.

The drag coefficient is determined from the Schiller and Naumann (1935) model correlation as

$$C_D = \begin{cases} 24\left(1+0.15\,\mathrm{Re}^{0.687}\right)/\mathrm{Re} & \mathrm{Re} \le 1000 \\ 0.44 & \mathrm{Re} > 1000 \end{cases} \tag{2.13}$$

The thermal energy conservation equation for a discrete phase particle can be written as

$$m_p c_p \frac{dT_p}{dt} = A_p \frac{\lambda Nu}{d_p}\left(T_g - T_p\right) + A_p \varepsilon_g \sigma_B \left(\theta_R^4 - T_p^4\right) + \sum_{k=1}^{N} \dot{m}_k \Delta h_k \tag{2.14}$$

Here, the rate of change in thermal energy of a particle is balanced by the convective and radiative heat transfer and heat due to chemical surface reactions. The convective heat transfer coefficient is determined from Ranz and Marshall's (1952) Nusselt number correlation

$$Nu = \frac{h d_p}{k_\infty} = 2.0 + 0.6\,\mathrm{Re}_d^{1/2}\,\mathrm{Pr}^{1/3} \tag{2.15}$$

The radiation temperature θ_R is found from the incident radiation G as $\left(G/4\sigma\right)^{1/4}$.

2.2 Coal Gasification

The gasification process can be broken down into the following simple sub-processes for ease of modeling. Coal (either dry feed or slurry feed) undergoes the following sub-processes during gasification (Shi et al, 2006).

2.2.1 Passive Heating

The coal particles are heated till the vaporization/devolatilization temperature is reached. There is no mass transfer or chemical reaction during this stage. When the coal particles reach a certain temperature, say the vaporization temperature, moisture is released. Accordingly, the moisture behaves as a source for the gas phase. Meanwhile, energy is taken out from the gas phase to supply the latent heat of vaporization. This stage is characterized by the absence of chemical reactions.

2.2.2 Devolatilization

A phenomenological model needs to be constructed based on data from experiments used to characterize the coal. This model can then be used to predict the yields of some major gas components while preserving a strict elemental balance to determine stoichiometry. The main species included in the devolatilization model are CH_4, CO_2, CO, O_2, H_2, H_2S, N_2 and H_2O.

The release of volatiles ($C_{m11}H_{m12}O_{m13}N_{m14}S_{m15}mois_{m17}$ or "Vol") from the coal can be represented as:

$$C_{m01}H_{m02}O_{m03}N_{m04}S_{m05}Ash_{m06}mois_{m07} \rightarrow C_{m11}H_{m12}O_{m13}N_{m14}S_{m15}mois_{m17} + C_{m21}Ash_{m26} \quad (2.16)$$

Here, *mois* represents the unbound water/water vapor contained in the feed particle.

The kinetic devolatilization rate is determined from the Kobayashi et al (1976) model with two-competing rates. The overall weight loss is determined by,

$$\frac{dm_v}{dt} = \left(m_{p,0} - m_a\right)\left(\alpha_1 R_1 + \alpha_2 R_2\right)\exp\left(-\int_0^t \left(R_1 + R_2\right)dt\right) \quad (2.17)$$

where, $R_1 = A_1 \exp\left(-E_1/RT_p\right)$ and $R_2 = A_2 \exp\left(-E_2/RT_p\right)$ are the two competing rates that control the devolatilization over different temperature ranges. The yield factors α_1 and α_2 represent devolatilization at low and high temperatures, respectively. The yield factors are feed specific and is determined from proximate analysis.

The Kobayashi model has been chosen over the constant rate, single kinetic rate and chemical percolation devolatilization (CPD) models. This is because, even though the CPD model is more comprehensive with a potential for improved results, the small incremental improvement is a harsh tradeoff for the increase in computation time/resources. The Kobayashi model has been proved to provide better results than the constant rate and single kinetic rate models for coal gasification and combustion.

2.2.3 Volatiles Oxidation, Char Combustion and Gasification

After all the volatiles have been released, oxidation of volatiles, char combustion and gasification takes place until all the char is consumed or the particles flow out of the reactor. The chemical reactions include volatile oxidation (combustion), char combustion (oxidation), char-steam gasification, char-carbon dioxide gasification and char-hydrogen gasification, followed by the gas phase reactions.

Volatiles oxidation/combustion for oxygen-rich conditions is given by,

$$C_{m11}H_{m12}O_{m13}N_{m14}S_{m15} + \left(m11 + \frac{m12}{4} - \frac{m13}{2} + m15\right)O_2 \xrightarrow{k1} m11CO_2 + \frac{m12}{2}H_2O + \frac{m14}{2}N_2 + m15SO_2 \quad (2.18)$$

Using the expression for the partial oxidation of volatiles from Chen et al (2000), we get the following equation for volatiles oxidation/combustion under oxygen-lean conditions $\left(\varphi < \left(m11 + \frac{m12}{4} - \frac{m13}{2} + m15\right)\right)$,

$$C_{m11}H_{m12}O_{m13}N_{m14}S_{m15} + \varphi O_2 \xrightarrow{k2} m11\left(\alpha_1 CO_2 + \alpha_2 CO\right) + \left(\frac{1-\alpha_1}{2}\left(m12 - 2m15\right)\right)H_2 + \frac{\alpha_1}{2}\left(m12 - 2m15\right)H_2O + \frac{m14}{2}N_2 + m15H_2S \quad (2.19)$$

Carbon monoxide and hydrogen are produced during the gasification of char particles. The performance of a gasifier is determined primarily by the char

gasification reaction. The following particle reactions have been included in the model,

$$C + \frac{1}{2}O_2 \xrightarrow{k3} CO \tag{2.20}$$

$$C + H_2O \xrightarrow{k4} CO + H_2 \tag{2.21}$$

$$C + CO_2 \xrightarrow{k5} 2CO \tag{2.22}$$

$$C + 2H_2 \xrightarrow{k6} CH_4 \tag{2.23}$$

The heterogeneous surface reactions are determined by a kinetics-diffusion limited reaction rate given by

$$\frac{dm_p}{dt} = -A_p p_{ox} D_0 \frac{k}{(D_0 + k)} \tag{2.24}$$

Here, the diffusion rate coefficient is given by (Field, 1969)

$$D_0 = C_1 \frac{\left[\frac{(T_p + T_\infty)}{2}\right]^{0.75}}{d_p} \tag{2.25}$$

and the kinetic rate for the heterogeneous reactions is given by,

$$k = C_2 e^{-(E/RT_p)} \tag{2.26}$$

2.2.4 Gas Phase Reactions

For most gasification studies using CFD, a reduced global reaction scheme was required in the past to make the computation possible in a realistic timeframe using limited computing and memory resources. This was one of the limitations imposed by the eddy-dissipation concept model, whereas for the finite-rate/eddy-dissipation model, a uniform turbulence rate for all the reactions was the limitation. To this end, various reduced schemes were proposed for combustion (and gasification) by Westbrook & Dryer (1981), Goyal & Gidaspow (1982) and Jones & Lindstedt (1988) to name but a few. Studies such as Chen et al (2001), Choi et al (2001), Liu et al (2002), Shi et al (2006), Watanabe & Otaka (2006) and Wu et al (2010) have used the three sources mentioned as well as others to form their reduced global reaction schemes. This study also employs a reduced global reaction scheme primarily taken from Westbrook & Dryer (1981), Jones & Lindstedt (1988), Chen et al (2001) and Wu et al (2010). More detailed reduced global reaction mechanisms for combustion (and gasfication) can be seen in sources such as Bradley et al (2001) and Alam et al (2010).

The continuous phase is modeled by using global reactions to describe gas phase chemistry. A set of global reduced reaction kinetics appropriate for gasification studies has been used in this analysis. The following reaction paths have been considered for this model

$$CH_4 + 0.5O_2 \xrightarrow{k7} CO + 2H_2 \qquad (2.27)$$

$$H_2 + 0.5O_2 \xrightarrow{k8} H_2O \qquad (2.28)$$

$$CO + 0.5O_2 \xrightarrow{k9} CO_2 \tag{2.29}$$

$$CO + H_2O \underset{k10b}{\overset{k10f}{\rightleftharpoons}} CO_2 + H_2 \tag{2.30}$$

Laminar finite-rate chemical kinetics and eddy-dissipation turbulence-chemistry interaction are combined to model the gas-phase reactions. The reaction rate of chemical species i due to the chemical reaction $R_{i,r}$ is taken as the sum of the reaction rates of r reactions that the species may take part in, that is,

$$R_i = \sum_r R_{i,r} \tag{2.31}$$

The effective reaction rate $R_{i,r}$ is given by the smaller of the laminar finite-rate and the eddy-dissipation reaction rates.

For a laminar non-reversible reaction r, the finite-rate reaction rate is given by Arrhenius chemical kinetics as

$$R_{i,r} = M_i \left(\upsilon''_{i,r} - \upsilon'_{i,r}\right) k_r \prod_j \left[C_{j,r}\right]^{\left(\eta'_{j,r} + \eta''_{j,r}\right)} \tag{2.32}$$

Here, $\upsilon'_{i,r}$ and $\upsilon''_{i,r}$ are stoichiometric coefficients for reactant and product species i, respectively. $C_{j,r}$ is the molar concentration of species j in reaction r. $\eta'_{j,r}$ and $\eta''_{j,r}$ are the rate exponents for reactant and product species j. M_i is the molecular weight of species i. The forward rate Arrhenius expression is given by

$$k_r = A_r T_g^{n_r} \exp\left(-\frac{E_r}{RT_g}\right) \tag{2.33}$$

Here A_r is the pre-exponential factor, E_r is the activation energy and n_r is the temperature exponent.

The eddy-dissipation reaction rate (Magnussen & Hjertager 1976) is given by the smaller/limiting-value of the following two expressions,

$$R_{i,r} = \upsilon'_{i,r} M_i A \rho \frac{\varepsilon}{k} \min_R \left(\frac{Y_R}{\upsilon'_{R,r} M_R}\right) \tag{2.34}$$

$$R_{i,r} = \upsilon'_{i,r} M_i AB \rho \frac{\varepsilon}{k} \frac{\sum_P Y_P}{\sum_P \upsilon''_{P,r} M_P} \tag{2.35}$$

Here, $\upsilon'_{R,r}$ and $\upsilon''_{P,r}$ are stoichiometric coefficients for reactant R and product P, respectively. Y_R and Y_P are the mass fractions of particular reactant and product species. A and B are empirical constants.

Two comments are necessary with respect to the gas phase reaction model. The first comment relates to the laminar finite-rate reaction rate which is strictly not applicable for turbulent reacting flows. It is introduced to get the reactions started when the turbulence level is low. Once, the chemical reactions are mixing-controlled, the eddy-dissipation model takes over. The second comment relates to the fact that the eddy-dissipation model cannot handle detailed chemical kinetics as all reactions have the same turbulence rate. Detailed chemical kinetics requires more advanced turbulent reaction models for instance like the eddy-dissipation concept (Magnussen 1981). Converged

solutions for such turbulent reaction models can be hard to achieve in particular for a stiff system of chemical reactions. Besides, numerical integration is considerably more expensive in terms of computer resources.

Two sets of chemical kinetics denoted Scheme 1 and 2 have been considered in this study. Scheme 1 given in Table 2.1 represents the chemical kinetics scheme used by Ajilkumar et al (2009) whom adapted their scheme from Chen et al (2000) for the heterogeneous reactions and Watanabe and Otaka (2006) for the gas-phase reactions. Scheme 2 given in Table 2.2 represents the chemical kinetics used by Wu et al. (2010) with some minor modifications.

Table 2.1. Rate Coefficients for Heterogeneous and Gas Phase Reactions – Coal (Scheme 1)

Eq. #	A_r	E_r *(J/kmol)*	n_r	$\prod_j \left[C_{j,r}\right]^{\left(\eta'_{j,r}+\eta''_{j,r}\right)}$	*Source*
(k1)	2.119 x 10^{11}	2.027 x 10^8	0	$[Vol]^{0.2}[O_2]^{1.3}$	FLUENT
(k2)	4.4 x 10^{11}	1.25 x 10^8	0	$[Vol]^{0.2}[O_2]^{1.3}$	Jones & Lindstedt (1988)
(k3)	0.052	6.1 x 10^7	-	-	Chen et al (2000)
(k4)	0.0782	1.15 x 10^8	-	-	Chen et al (2000)

(k5)	0.0732	1.125 x 10^8	-	-	Chen et al (2000)
(k8)	6.8 x 10^{15}	1.68 x 10^8	0	$[H_2]^1[O_2]^1$	Watanabe & Otaka (2006)
(k9)	2.2 x 10^{12}	1.67 x 10^8	0	$[CO]^1[O_2]^1$	Watanabe & Otaka (2006)
(k10f)	2.75 x 10^{10}	8.38 x 10^7	0	$[CO]^1[H_2O]^1$	Watanabe & Otaka (2006)
(k10b)	2.65 x 10^{-2}	3.96 x 10^3	0	$[CO_2]^1[H_2]^1$	Watanabe & Otaka (2006)

Table 2.2. Rate Coefficients for Heterogeneous and Gas Phase Reactions – Coal (Scheme 2)

Eq. #	A_r	E_r *(J/kmol)*	n_r	$\prod_j \left[C_{j,r}\right]^{\left(\eta'_{j,r}+\eta''_{j,r}\right)}$	*Source*
(k1)	2.119 x 10^{11}	2.027 x 10^8	0	$[Vol]^{0.2}[O_2]^{1.3}$	FLUENT adv. tut.
(k2)	4.4 x	1.25 x	0	$[Vol]^{0.2}[O_2]^{1.3}$	Jones &

	10^{11}	10^{8}			Lindstedt (1988)
(k3)	0.052	6.1×10^{7}	-	-	Chen et al (2000)
(k4)	0.0782	1.15×10^{8}	-	-	Chen et al (2000)
(k5)	0.0732	1.125×10^{8}	-	-	Chen et al (2000)
(k6)	6×10^{-7}	7.53×10^{7}	-	-	Govind & Shah (1984)
(k7)	4.4×10^{11}	1.25×10^{8}	0	$[CH_4]^{0.5}[O_2]^{1.25}$	Jones & Lindstedt (1988)
(k8)	2.5×10^{16}	1.68×10^{8}	-1	$[H_2]^{0.5}[O_2]^{2.25}[H_2O]^{-1}$	Jones & Lindstedt (1988)
(k9)	3.16×10^{12}	1.67×10^{8}	0	$[CO]^{1.5}[O_2]^{0.25}$	Wu et al (2010)
(k10f)	5×10^{12}	2.83×10^{8}	0	$[CO]^{0.5}[H_2O]^{1}$	Callaghan (2006)
(k10b)	9.5×10^{10}	2.39×10^{8}	0	$[CO_2]^{1}[H_2]^{0.5}$	Callaghan (2006)

2.3 Heavy Oil Gasification

Heavy oils are generally composed of a number of light and heavy hydrocarbons, with the heavier hydrocarbons typically represented by asphaltenes and maltenes. For ease of modeling, a simplified chemistry has been adopted in works such as Watanabe et al (2002) and Vaezi et al (2011). More detailed chemical reaction modeling has been handled in works such as Maki and Miura (1996), Mailybaev (2011), etc. These complex models using reduced global reaction schemes, but more comprehensive than in the first two sources mentioned, could be very interesting from the scope of future work.

Most of the modeling aspects discussed for coal gasification also holds true for heavy oil gasification. Gasification of heavy oil comprises the following sub-processes: passive heating, moisture evaporation, devolatilization, volatiles oxidation, char combustion, gasification and gas phase reactions. Volatiles oxidation/combustion is given for oxygen-rich conditions by

$$C_{m11}H_{m12}O_{m13}N_{m14}S_{m15} + \left(m11 + \frac{m12}{4} - \frac{m13}{2} + m15\right)O_2 \xrightarrow{k1} m11CO_2 + \frac{m12}{2}H_2O + \frac{m14}{2}N_2 + m15SO_2 \tag{2.36}$$

And, for oxygen-lean conditions by

$$C_{m11}H_{m12}O_{m13}N_{m14}S_{m15} + \varphi O_2 \xrightarrow{k2} m11\left(\alpha_1 CO_2 + \alpha_2 CO\right) + \left(\frac{1-\alpha_1}{2}\left(m12 - 2m15\right)\right)H_2 + \frac{\alpha_1}{2}\left(m12 - 2m15\right)H_2O + \frac{m14}{2}N_2 + m15H_2S \tag{2.37}$$

The particle surface reactions are given by

$$C + \frac{1}{2}O_2 \xrightarrow{k3} CO \tag{2.38}$$

$$C + H_2O \xrightarrow{k4} CO + H_2 \tag{2.39}$$

$$C + CO_2 \xrightarrow{k5} 2CO \tag{2.40}$$

The gas phase reactions are given by,

$$CO + H_2O \underset{k6b}{\overset{k6f}{\rightleftharpoons}} CO_2 + H_2 \tag{2.41}$$

$$CH_4 + H_2O \underset{k7b}{\overset{k7f}{\rightleftharpoons}} CO + 3H_2 \tag{2.42}$$

Table 2.3 represents a combination of the chemical kinetics scheme used by Watanabe et al (2002) and Maki and Miura (1997), with some minor modifications.

Table 2.3. Rate Coefficients for Heterogeneous and Gas Phase Reactions – Heavy Oil

Eq. #	A_r	E_r *(J/kmol)*	n_r	$\prod_j \left[C_{j,r}\right]^{\left(\eta'_{j,r}+\eta''_{j,r}\right)}$	*Source*
(k1)	2.119 x 10^{11}	2.027 x 10^{8}	0	$[Vol]^{0.2}[O_2]^{1.3}$	FLUENT (2010)

(k2)	4.4×10^{11}	1.25×10^{8}	0	$[Vol]^{0.2}[O_2]^{1.3}$	Jones & Lindstedt (1988)
(k3)	1.36×10^{6}	1.3×10^{8}	0.68	-	Watanabe et al (2002)
(k4)	2.07×10^{7}	2.2×10^{8}	0.733	-	Watanabe et al (2002)
(k5)	2.07×10^{7}	2.2×10^{8}	0.733	-	Watanabe et al (2002)
(k6f)	2.5×10^{5}	1.38×10^{8}	0	$[CO]^{1}[H_2O]^{1}$	Maki and Miura (1997)
(k6b)	9.4×10^{6}	4.12×10^{8}	0	$[CO_2]^{1}[H_2]^{1}$	Maki and Miura (1997)
(k7f)	9.1×10^{7}	1.31×10^{8}	0	$[CH_4]^{1}[H_2O]^{1}$	Maki and Miura (1997)
(k7b)	5.5×10^{-6}	1.76×10^{9}	0	$[CO]^{1}[H_2]^{3}$	Maki and Miura (1997)

All the other sub-models are identical to the ones discussed for the gasification of coal.

3. COAL GASIFICATION

This work focuses on CFD modeling of entrained-flow coal gasifiers of different scales, feedstocks and operating conditions. The CFD predictions are compared with relevant experimental data to validate how well the model captures the physical and chemical processes taking place within the gasifier.

3.1 Lab-Scale Oxygen-Blown Coal Gasifier

Soelberg et al. (1985) performed detailed space resolved measurements of gasification species products. Predictions using the coal gasification model are compared with their experimental data.

3.1.1 Gasifier Design

The gasifier geometry used in the lab-scale gasification experiments of Soelberg et al (1985) is illustrated in Figure 3.1. The length of the gasifier is 1.37m and its nominal diameter is 0.2m.

The design coal feed rate is 24.5kg/hr. The mass ratio of coal to oxygen to steam is 1.0:0.91:0.27. There are two streams entering the gasifier, the primary stream consists of a pre-mixture of oxygen and argon with coal, and the secondary stream consists of a mixture of steam and helium. The primary

stream was preheated to 366K and the secondary stream to 430K. The argon mass flow rate is 3.31kg/hr and that of helium is 0.076kg/hr.

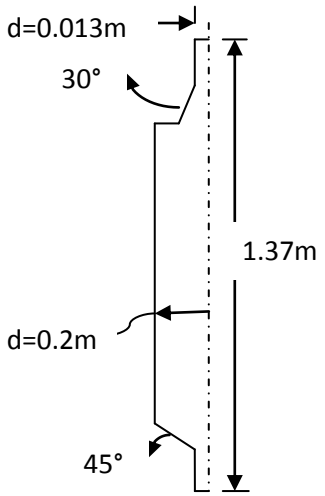

Figure 3.1: Schematic of gasifier geometry.

The coal particles were assumed to have a Rosin-Rammler size distribution with a minimum size of 4μm and a maximum of 76μm, with an average of 42μm. The spread parameter used was 1.2 and 10 discrete particle sizes were considered. Utah bituminous coal was considered, with the coal properties as given in Soelberg et al (1985). The stoichiomatric coefficients for Utah Bituminous coal as used in Eq. (2.19) are as given in Table 3.1.

Table 3.1: Utah bituminous coal – stoichiometric coefficient values.

Parameter	Value
m11	1.445
m12	3.538
m13	0.487
m14	0.064
m15	0.012

3.1.2 Modeling Details

The gasifier simulations were performed using the discrete phase method in FLUENT 12.1 on a 64-bit LINUX cluster utilizing 8 processors (2.3GHz). Gambit was used to generate the mesh for the 3D gasifier geometry consisting of 68070 tetrahedral elements. An average run consumed almost 48 hours for over 40,000 iterations to obtain solution convergence. The standard k-ε model was used for the continuous phase to model turbulence, and stochastic tracking was used for the steady-state model of the gasifier to simulate particle motion and turbulent dispersion. The SIMPLE algorithm was used to implement the pressure-velocity coupling with second-order upwind discretization.

Conductive, convective and radiative heat transfer was assumed between the gases, particles and reactor walls. The scattering property of the particles due to radiation is assumed to be isotropic and the standard P1 model has been used for the purpose of modeling radiative heat transfer. The weighted-sum-of-gray-gases-model (wsggm) was used to calculate the absorption coefficient of the gas

phase. Two-way coupling was assumed for turbulence interaction between continuous and discrete phases and, for heat and mass transfer.

3.1.3 Results and Discussion

The predictions are made with the first chemical kinetics scheme for coal comprising the heterogenous reaction rates of Chen et al. (2000) and the gas phase homogenous reactions of Watanabe and Otaka (2006).

The temperature profile and mole fraction distributions for carbon dioxide, carbon monoxide and hydrogen within the gasifier obtained from the FLUENT simulations were compared with the experimental results of Soelberg et al (1985). The entrained-flow gasifier was preheated to a temperature of between 1400K and 1700K with a methane pre-burner before the coal particles were injected. Hence, this temperature was patched to the gas phase before the simulation run was started.

The flow field velocity distribution within the gasifier shows strong downward flow at the inlet and outlet, and regions of recirculation near the top and side walls of the gasifier which is caused due to the high velocity of injection of the coal and oxygen. Below the recirculation regions, there is flow similar to plug flow – these classical flow characteristics have been observed in other gasification studies. The axial velocity profile is illustrated in Figure 3.2.

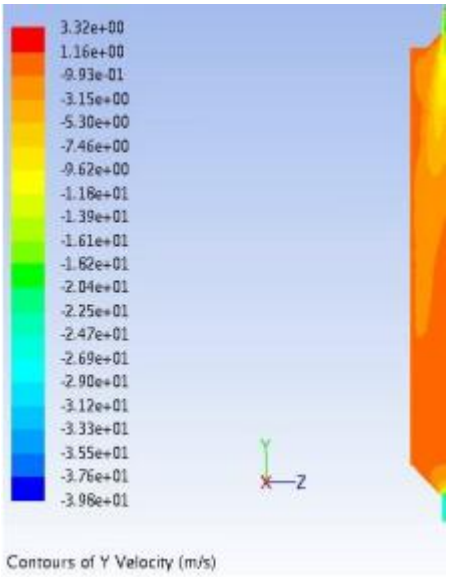

Figure 3.2: Axial velocity contour plot.

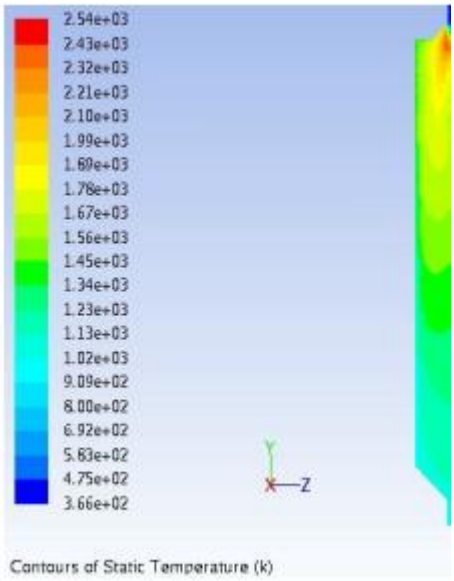

Figure 3.3: Temperature contour plot.

Figure 3.3 displays the temperature distribution within the gasifier obtained from the simulation. The highest temperature (about 2540K) is observed at the center, near the top of the gasifier (less than 0.1m from the top walls), which is primarily due to the process of combustion of the coal and oxidant. The combustion zone extends about 0.1m in the axial direction and below this zone the gas temperature decreases gradually as we move towards the outlet. This decrease in temperature is due to the gasification process which is an endothermic reaction consuming heat. The simulated peak temperature contour resembles the shape of a flame.

If we look at the mole fractions for the different species, there is good agreement with both the values and radial trends for carbon dioxide with the

experimental results as indicated in Figure 3.4. We see that the maximum deviation from the experimental values in this case occurs close to the inlet, and close to the axis of the gasifier. This variation could be attributed to high turbulence intensity in those regions, the physics of which the k-ε turbulence model captures weakly (especially in the presence of strong swirl). The difference in carbon dioxide mole fractions between the experimental data and the CFD predictions is a little over 6% at the outlet. The solid lines represent values from the FLUENT simulations while the markers represent the experimental data..

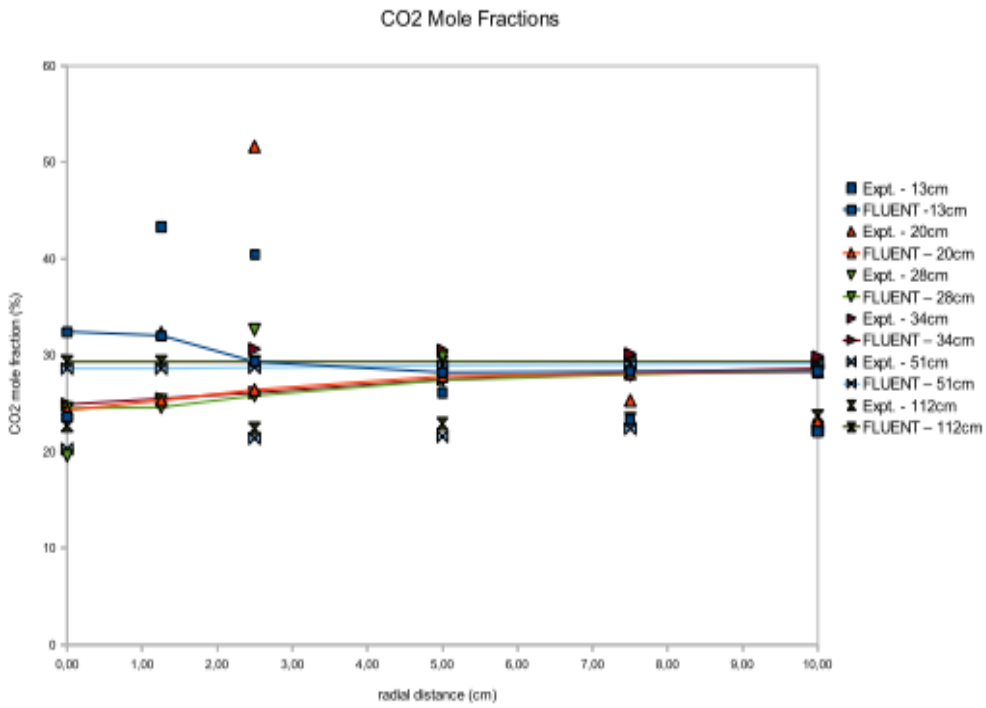

Figure 3.4: Radial profiles of CO_2 mole fraction.

In the case of carbon monoxide illustrated in Figure 3.5, we see an under-estimation of the production of CO, even though the model mostly captures the trends exhibited by the experimental data. The difference in carbon monoxide mole fractions between the experimental data and CFD predictions ranges between 15% and 18%.

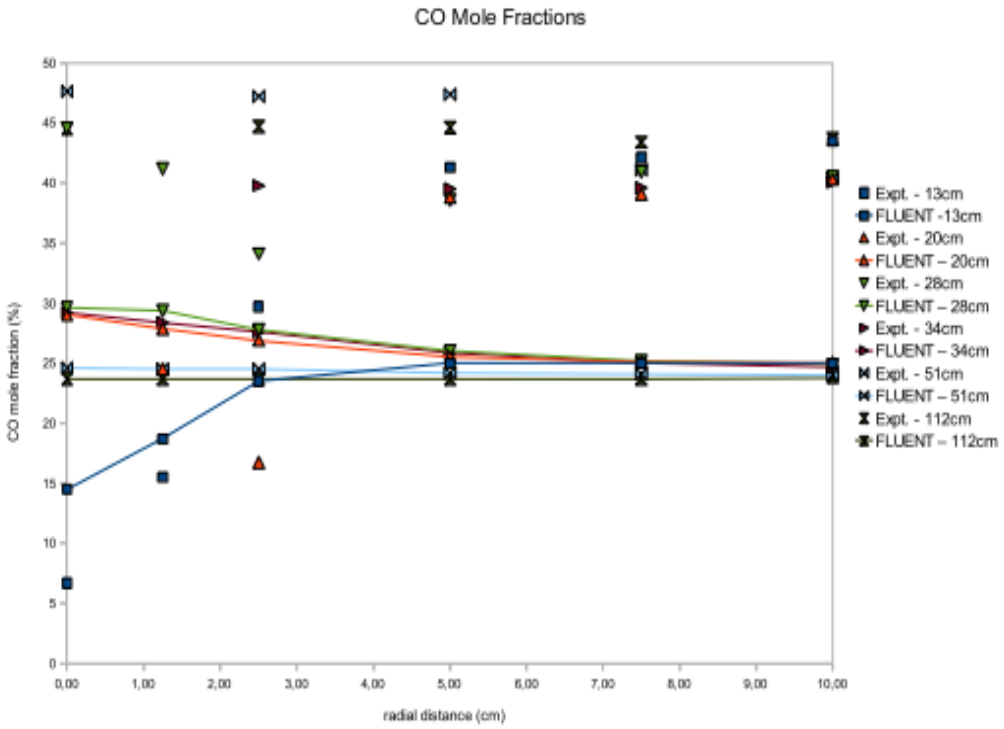

Figure 3.5: Radial profiles of CO mole fraction.

In the case of hydrogen illustrated in Figure 3.6, the experimental trends are seen to be captured, but the model over-estimates the mole fractions for different radial positions within the gasifier. The difference between the experimental and predicted mole fractions at the outlet of the gasifier varies between approximately 8% and 15%.

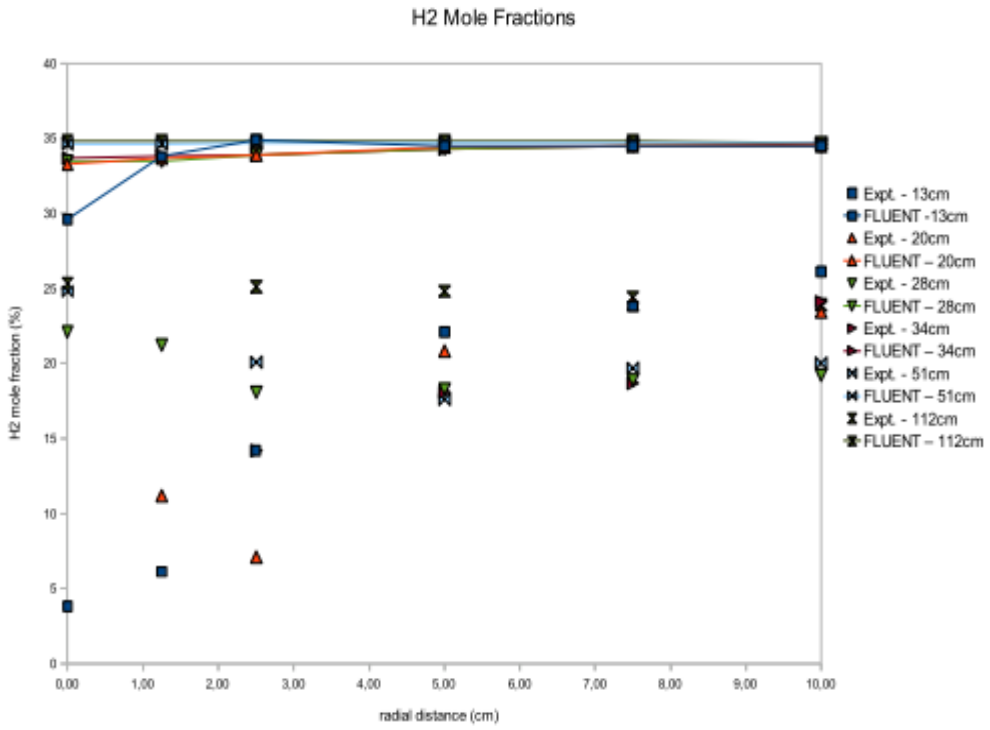

Figure 3.6: Radial profiles of H_2 mole fraction.

Whether the discrepancies in the radial species profiles are due to chemical kinetics or combustion modeling is hard to determine because measurements

characterizing the combustion zone is missing in the experiments conducted by Soelberg et al. (1985).

3.1.4 Concluding Remarks

When compared with the experimental data from Soelberg et al (1985), it is seen that the CFD model captures the radial trends for the molar fractions of carbon dioxide, carbon monoxide and hydrogen quite well. The absolute values of mole fractions at different radial locations within the gasifier are well-estimated for carbon dioxide, but the current model under-predicts the carbon monoxide mole fraction and over-predicts the hydrogen mole fraction.

Improvements are expected in the results from model refinements relating to the chemical kinetics, detailed modeling of the gasifier inlet, numerical schemes including the turbulence model, inclusion of swirl, radiation models used and mesh refinement. The best agreement with experimental data has been obtained for the mole fraction of carbon dioxide and the worst with carbon monoxide.

Whether the discrepancies in the radial species profiles are due to chemical kinetics or combustion modeling is hard to determine because measurements characterizing the combustion zone is missing in the experiments conducted by Soelberg et al (1985).

3.2 Idealized Lab-Scale Air-Blown Coal Gasifier

Ajilkumar et al (2009) proposed an idealized lab-scale coal gasifier to validate their numerical model against the experimental data of Watanabe and Otaka (2006). This work in turn uses the same gasifier design to see how the two proposed chemical kinetics schemes perform.

3.2.1 Gasifier Design

A schematic of the gasifier layout is given in Figure 3.7. The tubular gasifier has a length of 1m and a nominal diameter of 0.072m.

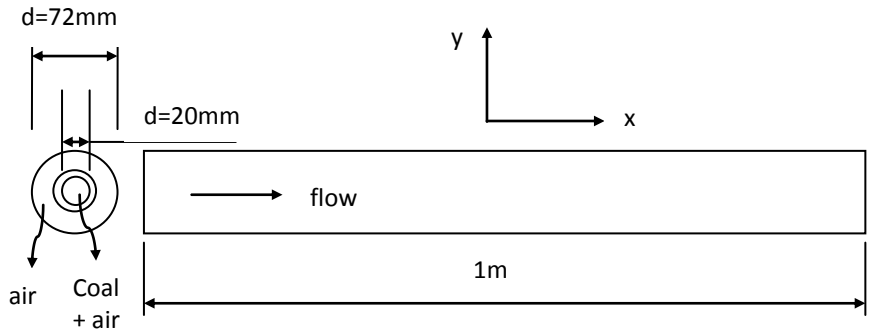

Figure 3.7: Schematic of gasifier geometry.

The gasifier has two inlet streams. Coal particles and primary air is fed centrally through a tube with an inner diameter of 20 mm. The coal feed rate is 2.4 kg/h. Secondary air is fed through the annulus between the inlet tube and the gasifier tube. The gas ratio defined as the total air fed to the gasifier to the air required

for complete combustion of coal on a mass basis is 0.409. The coal inlet stream was preheated to 400K and the outer stream to 600K. The operating pressure for this gasifier is 2MPa.

The proximate and ultimate analysis for the Australian black coal (coal M) used is given in Table 3.2.

Table 3.2: Coal M - proximate and ultimate analyses.

	(Wt. %)
Proximate analysis	
Moisture	4.2
Fixed Carbon	56.2
Volatile Matter	30.9
Ash	8.7
Ultimate analysis	
Carbon	76.3
Hydrogen	5.31
Nitrogen	1.54
Oxygen	7.31
Sulfur	0.46

The stoichiometric coefficient values for the volatiles content of coal M are given in Table 3.3, below.

Table 3.3: Coal M – stoichiometric coefficient values.

Parameter	Value
m11	1.53
m12	3.43
m13	0.46
m14	0.043
m15	0.0036

The feed rates of the coal and air make it an oxygen-lean environment within the gasifier.

The coal particles are assumed to fit a Rosin-Rammler size distribution with a minimum diameter of 4μm, a maximum diameter of 140 μm and an average diameter of 54.5μm. The spread parameter is 2.51, and 6 discrete particle sizes are considered.

3.2.2 Modeling Details

The discrete phase method in FLUENT 12.1 was used for the CFD simulation. The computational mesh consists of 72 x 1000 quadrilateral control volume elements. Axisymmetry had been assumed for the model computation and suitable 2D axisymmetry boundary conditions were applied.

The standard k-ε model was used for modeling turbulence in the continuous phase, and stochastic tracking was implemented for the steady-state model of the gasifier to simulate particle motion and turbulent dispersion. The SIMPLE algorithm was used to implement the pressure-velocity coupling with second-order upwind discretization. Conductive, convective and radiative heat transfer was assumed between the gases, particles and reactor walls. The scattering property of the particles due to radiation is assumed to be isotropic and the standard P1 model has been used for the purpose of modeling radiative heat transfer. This model is based on the expansion of radiation intensity into an orthogonal series of spherical harmonics. The weighted-sum-of-gray-gases-model (wsggm) was used to calculate the absorption coefficient of the gas phase. Two-way coupling was applied for both the turbulence model and heat and mass transfer computations.

3.2.3 Results and Discussion

The first chemical kinetics scheme considered comprises the heterogeneous reaction rates of Chen et al (2000) and the gas-phase reaction rates of Watanabe and Otaka (2006). This scheme is denoted Scheme 1. The reactive flow in the gasifier is illustrated by contour plots of the temperature distribution in Figure 3.8 and the velocity distribution in Figure 3.9.

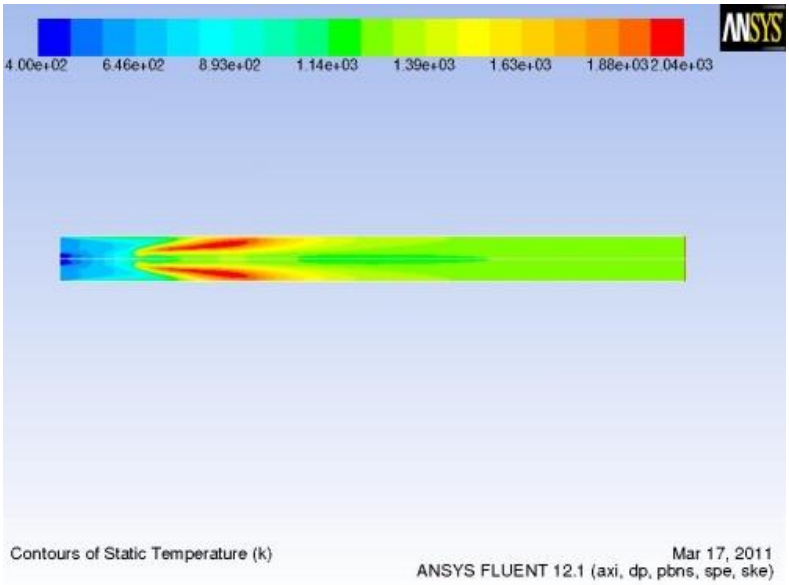

Figure 3.8: Temperature contour plot - Scheme 1.

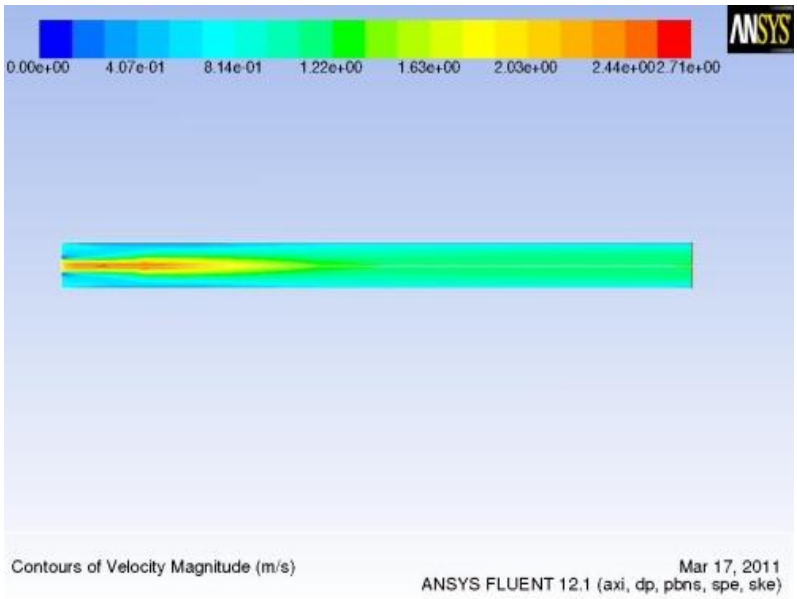

Figure 3.9: Velocity contour plot - Scheme 1.

The maximum temperature within the gasifier is approximately 2042K and occurs 0.2m downstream of the inlet. The maximum velocity is estimated to be 2.71m/s, and occurs along the gasifier axis.

The chemical reactions in the gasifier are illustrated by contour plots of the mole fraction of carbon monoxide in Figure 3.10 and hydrogen in Figure 3.11. The mole fraction at the gasifier outlet varies between 17% and 20 % for carbon monoxide and around 11% for hydrogen. The peak mole fraction is 31.4% for carbon monoxide and 16% for hydrogen.

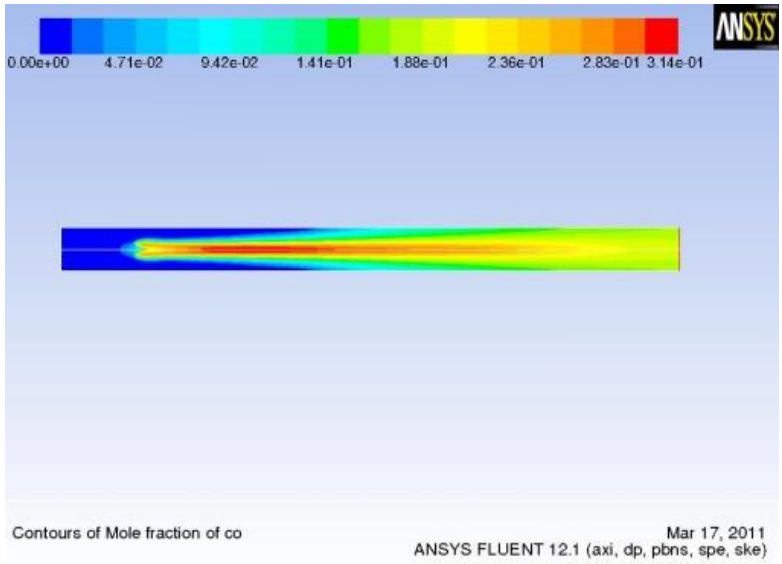

Figure 3.10: CO mole fraction contour plot – Scheme 1.

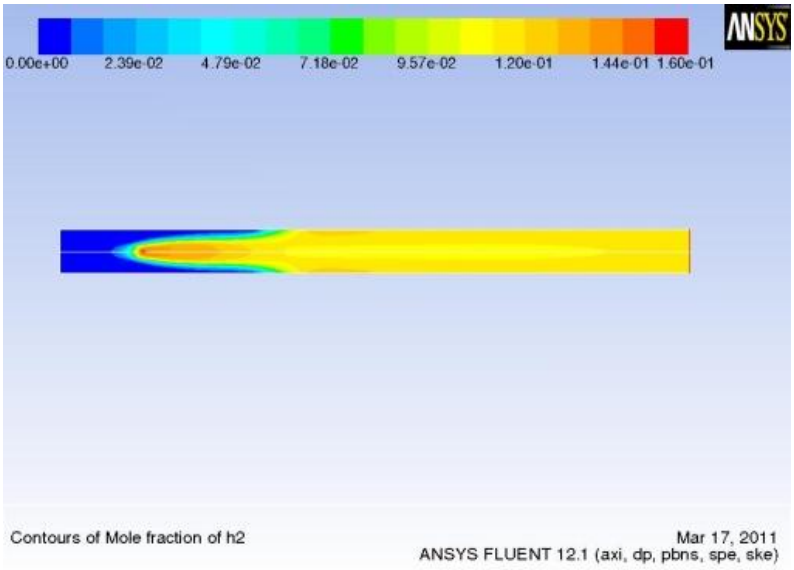

Figure 3.11: H_2 mole fraction contour plot – Scheme 1.

The second chemical kinetics scheme considered comprises the heterogeneous reaction rates of Chen et al (2000) and the gas-phase reaction rates of Wu et al (2010) and Callaghan (2006). This scheme is denoted Scheme 2. The reactive flow in the gasifier is illustrated by contour plots of the temperature distribution in Figure 3.12. The velocity contour plot is not depicted since it is almost identical to the plot obtained with the first scheme.

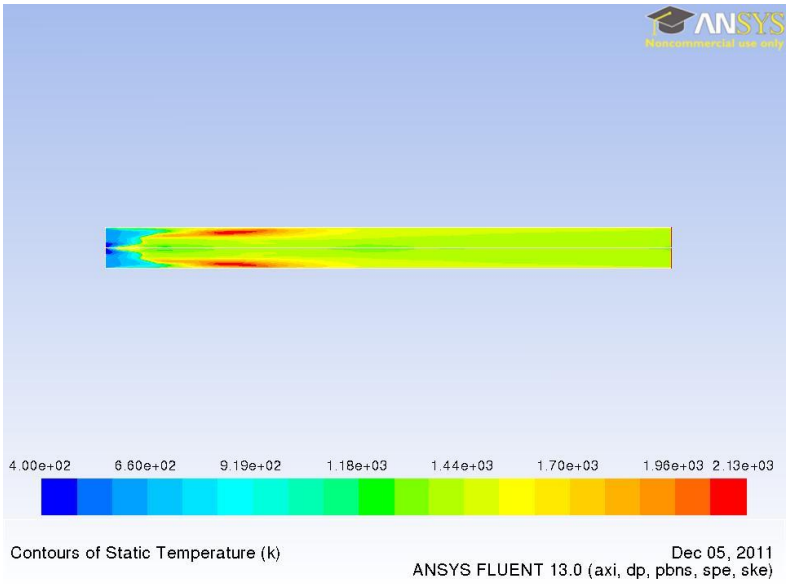

Figure 3.12: Temperature contour plot – Scheme 2.

The peak temperature observed is about 2130K, which is higher than that obtained with the first scheme, at an almost identical location within the gasifier.

The chemical reactions in the gasifier are depicted by contour plots of the mole fraction of carbon monoxide in Figure 3.13 and hydrogen in Figure 3.14. The mole fraction at the gasifier outlet varies between 19.6% and 21 % for carbon monoxide and around 7.5% for hydrogen. The peak mole fraction is 32.3% for carbon monoxide and 13% for hydrogen.

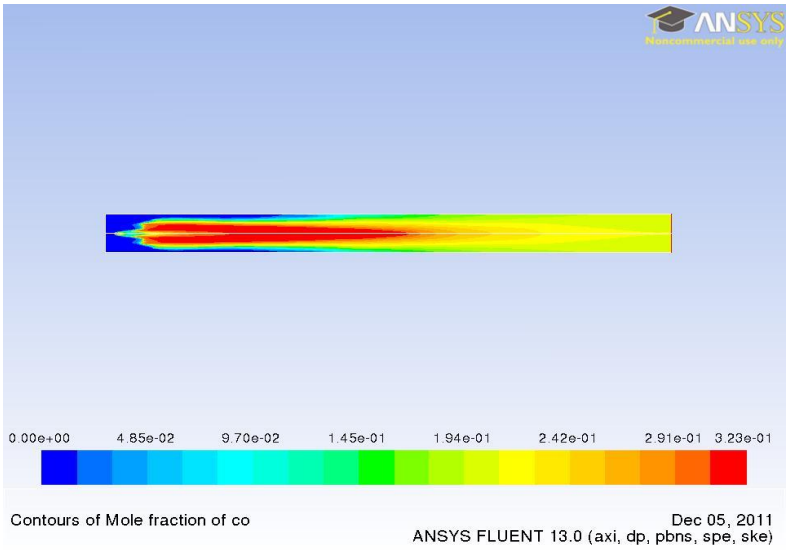

Figure 3.13: CO mole fraction contour plot - Scheme 2.

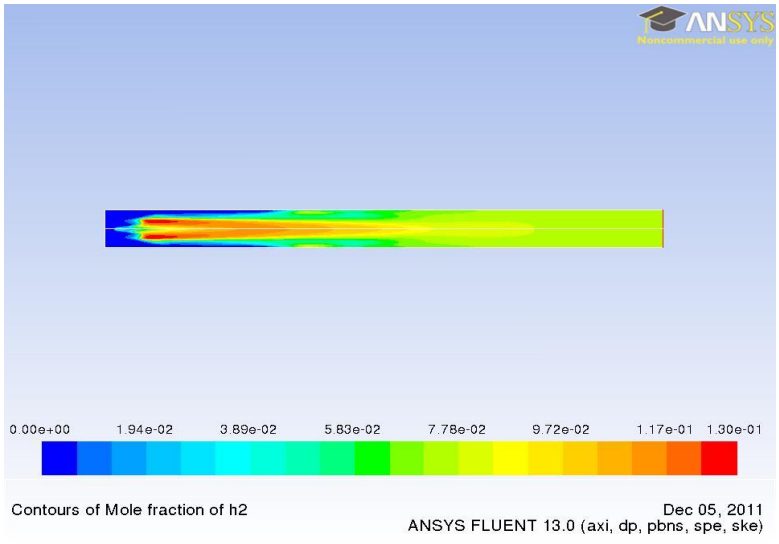

Figure 3.14: H_2 mole fraction contour plot – Scheme 2.

The temperature profile along the gasifier axis and in the gasifier flow direction is shown in Figure 3.15. The predictions with the two chemical kinetics schemes are compared with the numerical results of Ajilkumar et al. (2009) and the experimental data of Watanabe and Otaka (2006). As indicated by the temperature contour plots, it should be noted that the maximum temperature does not occur along the central axis of the gasifier.

It can also be observed that the agreement with experimental results is dissimilar for all the CFD studies depicted with the correct temperature trend being captured in the axial direction with Scheme 2. It is hard to say much about the maximum temperature within the gasifier since there is just one experimental data point in proximity with the combustion zone of the gasifier. However, some information is conveyed downstream of the combustion and gasification zone by additional data points, and some comparison can be made with these. Scheme 2 and Ajilkumar et al (2009) estimate similar temperature trends at the points where experimental data is available, with their absolute temperature values being in proximity as well. However, scheme 1 predicts the best gasifier outlet temperature followed by scheme 2. If we do consider the lone data point close to the combustion zone, the temperature trend and the outlet temperature, scheme 2 performs the best with respect to gasifier axis temperature estimates.

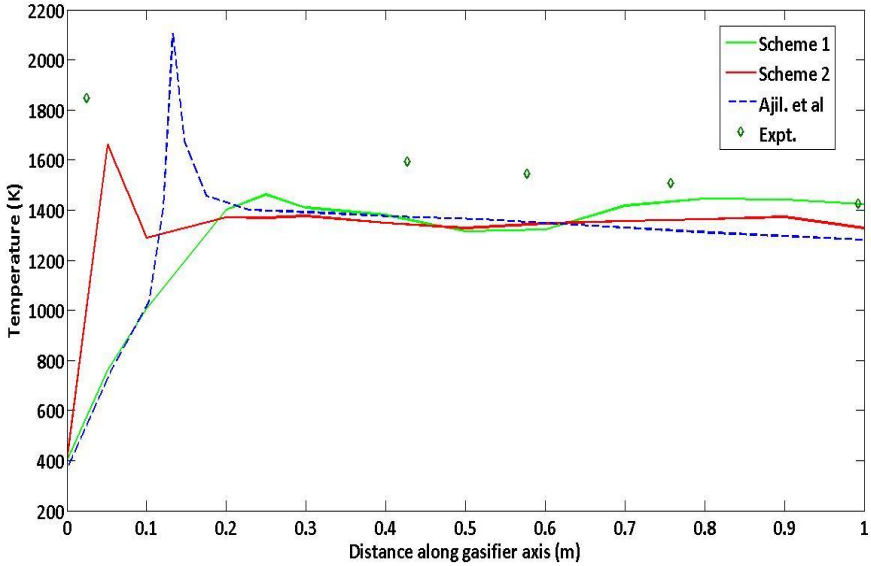

Figure 3.15: Temperature along gasifier axis.

The mole fractions for the major species at the gasifier outlet are shown in Figure 3.16. The predictions with the two chemical kinetics schemes are again compared with the numerical results of Ajilkumar et al. (2009) and the experimental data of Watanabe and Otaka (2006).

In comparison with the experimental data, the second chemical kinetics scheme, scheme 2, is seen to perform better than the first chemical kinetics scheme, scheme 1. Scheme 2 performs also marginally better than the predictions of Ajilkumar et al. (2009). This is particularly so for carbon monoxide and water vapor. The species mole fraction errors for scheme 1 vary from 1.5% for carbon monoxide to 76.5% for hydrogen. Scheme 1 is not able to predict the outlet

mole fraction for water vapor. The species mole fraction errors for scheme 2 vary from 1.5% for carbon monoxide to 15.4% for hydrogen.

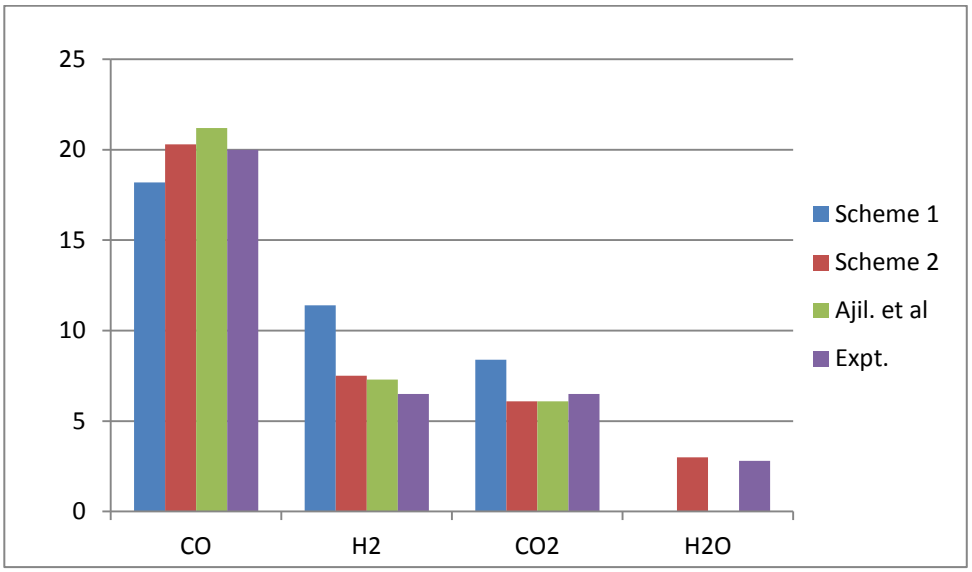

Figure 3.16: Species mole fraction % at gasifier outlet.

The species mole fractions along the gasifier axis for the two chemical kinetics schemes are compared with Ajilkumar et al (2009) in Figure 3.17 for carbon dioxide and carbon monoxide and in Figure 3.18 for hydrogen.

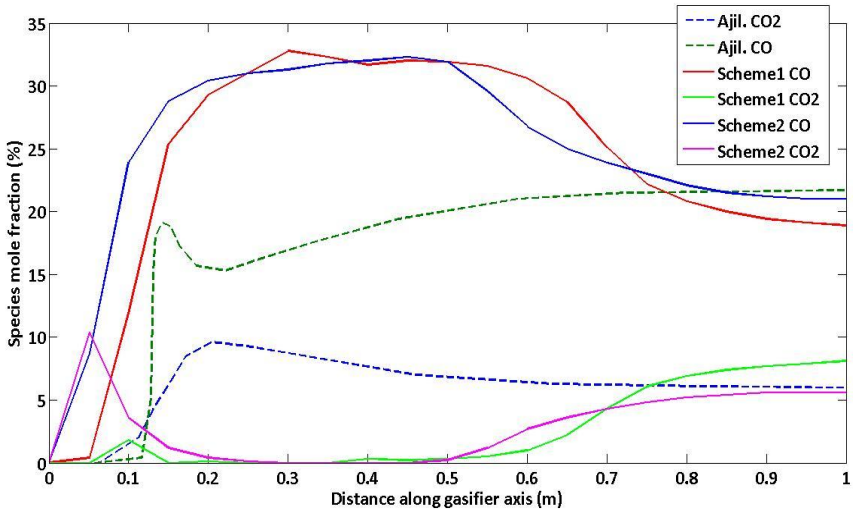

Figure 3.17: CO and CO_2 mole fractions along gasifier axis.

One reason for the early increase in carbon dioxide production could be the consumption of oxygen by the released volatiles. Further downstream, there is a balance between the homogeneous gas phase reactions and the heterogeneous surface reactions. Hence, carbon dioxide decreases and carbon monoxide increases as the volatiles consume oxygen. Nearing the outlet, again the mole fraction of carbon dioxide begins to increase and carbon monoxide begins to decrease.

It is seen that the outlet mole fractions of both schemes are similar, with a similar trend along the gasifier axis for the mole fraction of carbon monoxide. However, it appears that there is pronounced peak close to the inlet (0.05m) for the carbon dioxide mole fraction in scheme 2 (about 10%) which is not observed with scheme 1. It appears that the axial profiles for the mole fractions

of these two species for the two schemes are quite different compared with the results of Ajilkumar et al (2009). The peak mole fraction for carbon monoxide observed by Ajilkumar et al (2009) within the gasifier is about 30% less than that predicted by the two schemes. At a distance of 0.3 to 0.5m from the inlet, the peak value for the species mole fraction for carbon monoxide is observed for the two schemes whereas in the case of Ajilkumar et al (2009) this maximum is observed close to the gasifier outlet. In the case of carbon dioxide at the same axial distance downstream of the inlet, the minimum of its mole fraction is observed for the two schemes whereas a maximum is observed for Ajilkumar et al (2009) about 0.2m downstream of the inlet. In other words, between 0.15m and 0.75m from the gasifier inlet (along its axis), the two schemes predict more carbon monoxide and less carbon dioxide than Ajilkumar et al (2009).

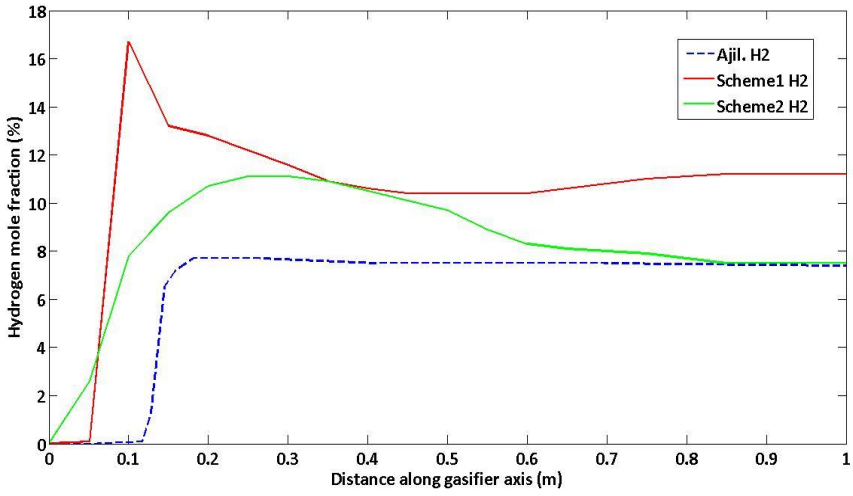

Figure 3.18: H_2 mole fraction along gasifier axis.

From Figure 3.18 it is seen that the hydrogen mole fraction predicted by scheme 1 is high when compared to the predictions of the other two CFD models. Scheme 2 produces results that shows good agreement with experimental data, and can be deemed more suitable than scheme 1. Both scheme 2 and Ajilkumar et al (2009) predict almost the same mole fraction percentage for hydrogen at the gasifier outlet.

3.2.3 Concluding Remarks

It is seen that scheme 1 is unable to correctly predict the temperature distribution along the gasifier axis, while scheme 2 performs the task admirably. The peak temperature observed with scheme 1 is 2042K, whereas with scheme 2 a peak temperature of 2130K is predicted. The location and extent of the combustion zone is estimated well by scheme 2 while scheme 1 fails in this regard.

It is also observed that scheme 2 produces more accurate results when investigating the gasifier outlet species mole fractions. The over-prediction of hydrogen and the non-prediction of water vapour is a small concern with scheme 1. It was observed that both devolatilization and char burnout were most active in a region close to the inlet, between 0.06m and 0.1m from the inlet in the axial direction. This corresponds well with the location where the carbon dioxide is found to be a maximum close to the inlet in scheme 2.

From the predictions of temperature distribution and species mole fractions at the gasifier outlet, it can be concluded that the performance of scheme 2 makes it a suitable candidate for use in future studies of coal gasification.

3.3 MHI-type Pilot-Scale Air-Blown Coal Gasifier

Chen et al. (2000) performed a study on a 200 t/d pilot-scale air blown entrained-flow gasifier of the Mitsubishi Heavy Industries type. The present CFD predictions are compared with their experimental and numerical data.

3.3.1 Gasifier Design

The two-stage up-flow gasifier studied by Chen et al. (2000) with its main dimensions is illustrated in Figure 3.19.

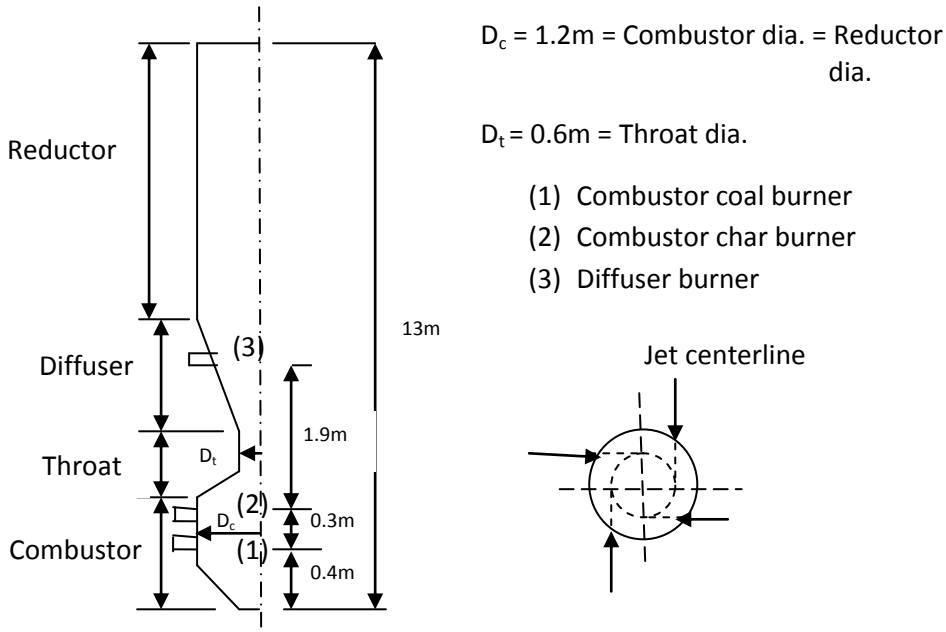

Figure 3.19: Schematic of the gasifier used by Chen et al (2000).

Pulverized coal together with air is injected into the combustor at the inlet nozzles (1) and into the reductor at the inlet nozzles (3). Recycled char together with air is injected into the combustor at the inlet nozzles (2). The inlet nozzles are arranged tangentially to give a swirling flow in the gasifier. The coal and air feed rates are given in Table 3.4.

Table 3.4: Coal and air feed rates.

Gasifier inlet	Coal feed rate (kg/s)	Air feed rate (kg/s)
Combustor coal burner	0.472	4.708
Char burner	1.112	4.708
Reductor coal burner	1.832	1.832

The coal particle velocity at injection is 3 m/s. The air is assumed to be comprised of 23% by weight of oxygen, the rest being nitrogen (and non-reacting gases). The coal used is Taiheiyo bituminous coal. The proximate & ultimate analysis and the stoichiometric coefficient values of this coal's volatile content are given in Table 3.5 and Table 3.6, respectively.

Table 3.5: Taiheiyo Coal - proximate and ultimate analyses.

Proximate analysis	**Wt. %**
Moisture	5.3
Fixed Carbon	35.8
Volatile Matter	46.7
Ash	12.1
Ultimate analysis	**Wt. %**
Carbon	77.6
Hydrogen	6.5
Nitrogen	1.13
Oxygen	13.9
Sulfur	0.22

Table 3.6: Stoichiometric coefficient values for the coal used.

Parameter	Value
m11	1.53
m12	3.43
m13	0.46
m14	0.043
m15	0.0036

A Rosin-Rammler size distribution is assumed for the coal particles to account for the non-uniformities in particle size after pulverizing or grinding. The parameters for this distribution are given in Table 3.7.

Table 3.7: Coal particle size distribution parameters

Parameter	**Value**
Distribution Type	Rosin-Rammler
Minimum Diameter	4µm
Maximum Diameter	150µm
Mean Diameter	39.8µm
Spread Parameter	1.2
No. of Diameters	6
No. of Coal Particle Packets	29424

Following Chen et al. (2000), the wall temperatures are kept fixed adopted to account for heat losses and heat cooling effects. The wall temperatures are maintained at 1849K in the combustor, 1073 K in the diffusor and 873 K in the reductor. The operating pressure of the gasifier is 2.7MPa.

3.3.2 Modeling Details

The discrete phase method in FLUENT 12.1 was used for the CFD simulation. The computational mesh consists of 70312 tetrahedral control volume elements in a fully three-dimensional computational domain. The steady-state, pressure-based solver was adopted in three dimensions. Pressure-velocity coupling was implemented using the SIMPLE algorithm with a Green-Gauss cell based method and a second-order upwind spatial discretization scheme. The standard k-ε model was implemented for modeling turbulence. An Euler-Lagrange description of the flow was used with the discrete phase method (DPM) in which the coal particles represent the discrete phase and the continuous phase is represented by the gas phase. To model the interaction of the discrete and continuous phases, two-way coupling of momentum, turbulence, heat and mass transfer between the phases was employed.

3.3.3 Sensitivity Analysis

Parameter sensitivity analysis was conducted with respect to mesh refinement, with the finer mesh then utilized to compare one- and two-way coupling for

heat and mass transfer between the continuous and discrete phases and for adiabatic wall conditions versus fixed wall temperatures.

There was a small difference observed in peak temperatures between the coarse (47265 tetrahedral control volume elements) and fine mesh (70312 tetrahedral control volume elements). The peak temperature in the fine mesh case was predicted as approximately 2294K compared to 2253K for the coarse mesh case (error of 1.8%). Two-way heat and mass transfer coupling yields a peak temperature of around 2317K with the fine mesh and fixed wall temperatures. A simulation run with one-way coupling converged in approximately 40 hours, while with two-way coupling, the same case consumed almost 190 hours before convergence. Application of adiabatic wall conditions yielded a maximum temperature of around 2380K within the gasifier.

Based on these results, two-way heat and mass transfer coupling (with momentum and turbulence interchange between the phases) was chosen along with the fine computational mesh and fixed wall temperatures.

3.3.4 Results and Discussion

The reactive flow is first illustrated for the first chemical kinetics scheme (scheme 1), which comprises the heterogeneous reaction rates from Chen et al (2000) and gas-phase reaction rates from Watanabe and Otaka (2006). Contour plots of temperature and velocity are shown in the middle of the gasifier with cross-planes for the inlets in the combustor and reductor. The temperature distribution is shown in Figure 3.20.

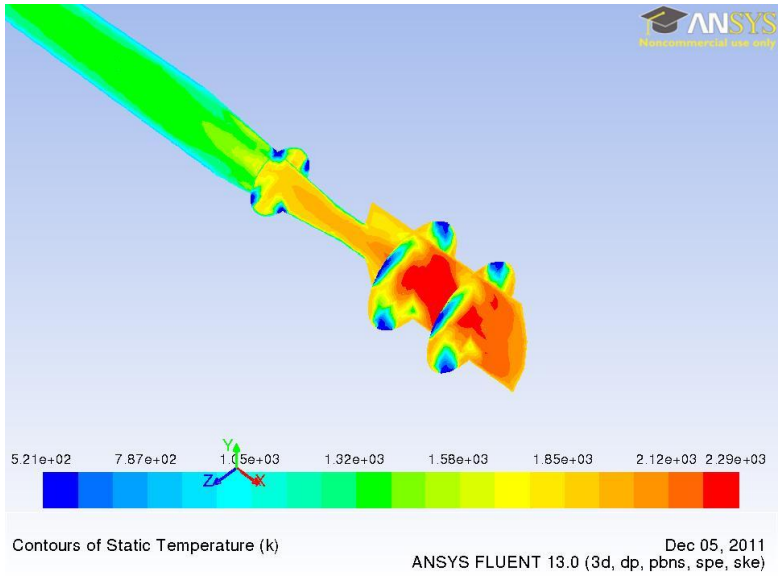

Figure 3.20: Temperature contour plot - Scheme 1.

A peak temperature of approximately 2294K is observed centrally in the gasifier between the two combustor inlets. The velocity distribution is shown in Figure 3.21 for a velocity scale representative for the gasifier flow and in Figure 3.22 for a velocity scale representative for the inlet flow.

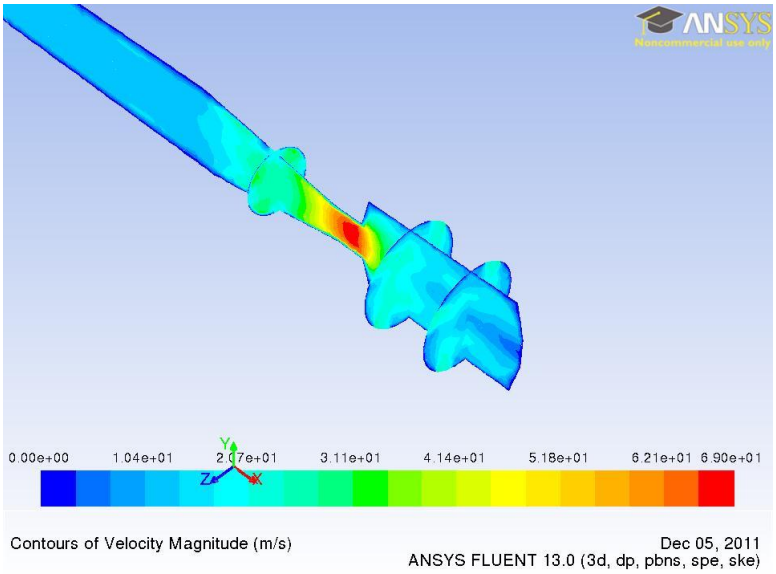

Figure 3.21: Velocity contour plot – Scheme 1.

A maximum velocity of about 69m/s is observed in the "throat" region between the combustor and reductor of the gasifier. A swirling flow pattern is clearly seen in the inlet planes of the combustor and the reductor.

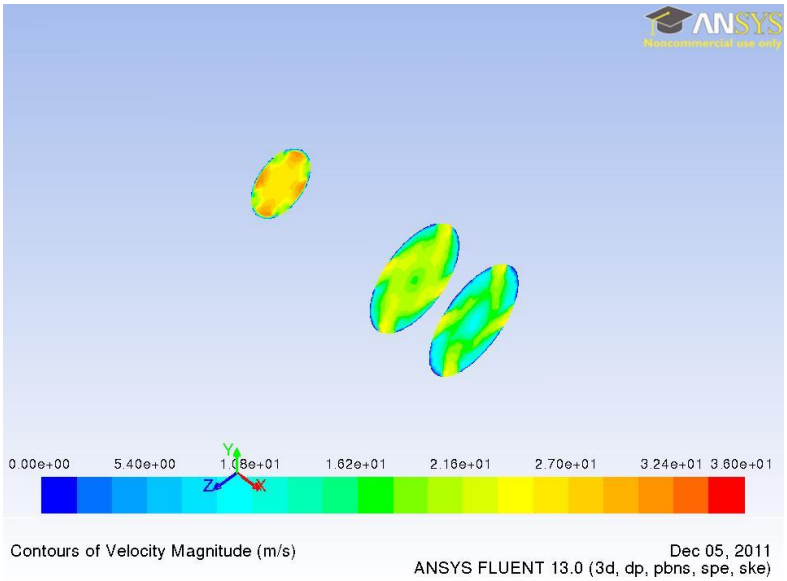

Figure 3.22: Velocity plots at combustor and diffuser inlets – Scheme 1.

The reactive flow is next illustrated for the second chemical kinetics scheme (Scheme 2), which comprises the heterogeneous reaction rates from Chen et al (2000) and of gas-phase reaction rates of Wu et al (2010) and Callaghan (2006). A contour plot of the temperature is shown in Figure 3.23. A peak temperature of approximately 2237K is observed centrally in the gasifier between the two combustor inlets. Accordingly the peak temperature is slightly lower for scheme 2 compared to scheme 1. The velocity distribution is similar for the two chemical kinetics schemes.

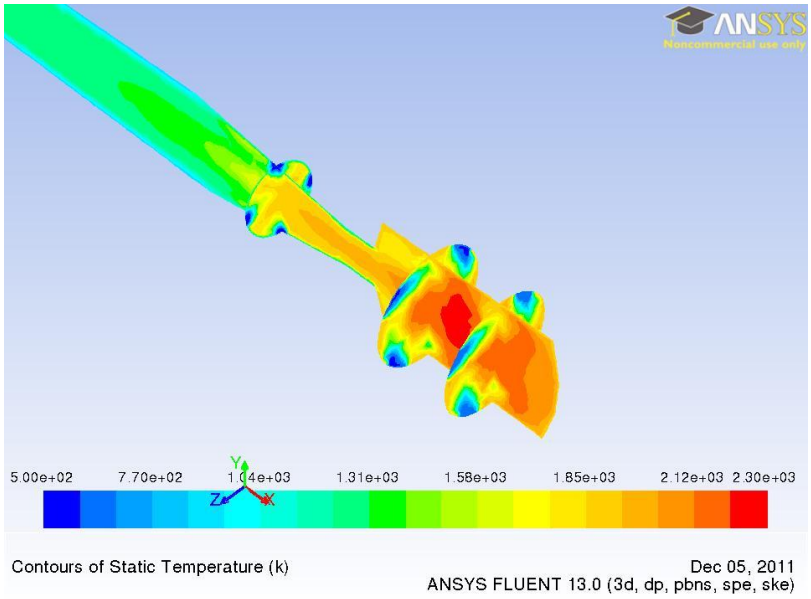

Figure 3.23: Temperature contour plot – Scheme 2.

A more interesting comparison can be made by observing the mole fractions of the major product species at the gasifier outlet as illustrated in Figure 3.24. Comparison with experimental data reveals which of these two reduced global reaction schemes yield predictions best suited for the net effect of the large number of reactions taking place within the gasifier.

Both chemical kinetics schemes are seen to offer predictions that are in good agreement with experimental data. So do the predictions of Chen et al. (2000). Scheme 2 appears to offer marginally better predictions than Scheme 1 with respect to carbon monoxide and carbon dioxide. With respect to hydrogen, the deviation from the experimental value is comparable for both schemes, but in opposite directions. The present predictions show the comparable results as the

predictions of Chen et al. (2000). To provide a quantitative feel for the outlet species mole fractions, we compare the errors in the Chen et al (2000) and scheme 2 predictions. We see that the error for CO is about 6% for scheme 2 and 4% for Chen et al (2000), for H_2 it is approximately 20% for both scheme 2 and Chen et al (2000), and for CO_2 is about 4% for scheme 2 and 12% for Chen et al (2000).

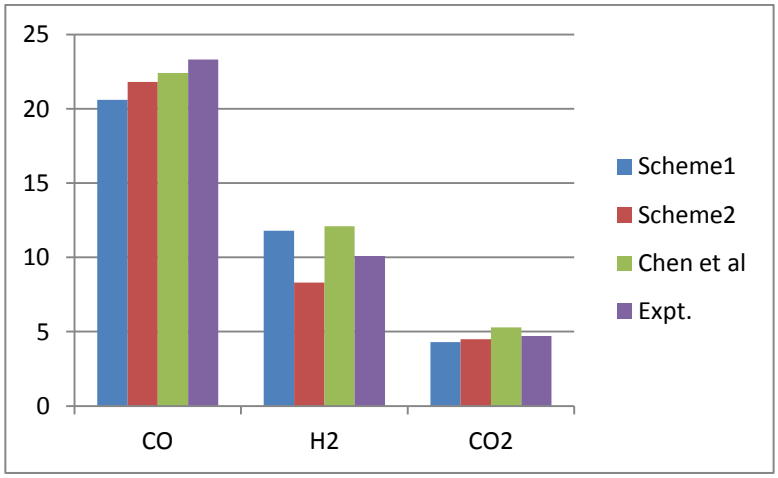

Figure 3.24: Species mole fraction % at gasifier outlet.

Figure 3.25 displays the variation of temperature along the gasifier axis in the combustor and throat regions of the gasifier. This plot is significant because close agreement with experimental data signifies a good prediction of the flow field, realistic modeling of the turbulence and chemistry interaction including the combustion and gasification process. Again, it is quite difficult to estimate the peak temperature within the gasifier from the experimental data due to lack

of data points in the combustion zone. However, an intelligent guess can be hazarded that it most likely lies between the 0.28m and the 1m axial data points. The temperature "drop off" along the gasifier axis is much more rapid in the predictions of Chen et al (2000) as compared to the predictions of either scheme 1 or scheme 2. None of the predictions follow the exact axial temperature trend displayed in the experiment; however scheme 2 comes closest to doing that. Therefore, it can be concluded that scheme 2 provides the best agreement with experimental data both in terms of the axial trend and absolute values of temperature.

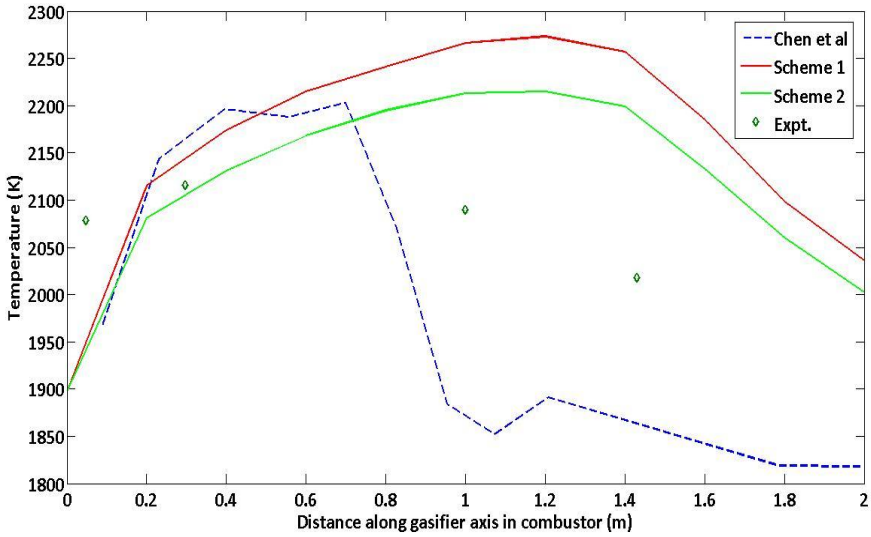

Figure 3.25: Temperature along gasifier axis.

Using both Figure 3.24 and Figure 3.25, it is seen that scheme 2 offers the most realistic predictions. In other words, scheme 2 best reflects the different physical and chemical processes taking place within the gasifier – particularly the reduced global chemical reaction scheme and the interaction of turbulence and chemistry. With the use of scheme 2, an incremental improvement over the predictions of Chen et al (2000) was observed.

3.3.5 Concluding Remarks

It is seen that both the chemical kinetics schemes illustrated in this study perform admirably well for the gasifier design in Chen et al (2000) both in terms of the predicted temperature distribution within the gasifier as well as the species mole fractions of the product syngas measured at the gasifier outlet.

It is clear that the temperature was not measured in the combustion zone at or near the location of the peak temperature in the experimental work done by Chen et al (2000). However, it is seen that at the measurement point closest to the combustion zone, the errors in estimation provided by the three sets of numerical predictions are 3%, 1.5% and 0.7% by Chen et al (2000), scheme 1 and scheme 2, respectively.

With respect to the model described by Chen et al (2000), the chemical reaction kinetics scheme 2 provides the best estimate, both with respect to the species mole fractions of the product syngas as well as the temperature distribution observed along the gasifier axis as discussed earlier.

3.4 MHI-type Lab-Scale Coal Gasifier (CRIEPI)

Watanabe and Otaka (2006) performed a study on a 2t/d lab-scale air blown entrained-flow gasifier. The present CFD predictions are compared with their experimental and numerical data. The 200t/d pilot-scale gasifier studied by Chen et al. (2000) and presented in Chapter 3.3 is a scale-up of the 2t/d lab-scale gasifier studied by Watanabe and Otaka (2006).

3.4.1 Gasifier Design

The mesh for the second model (Watanabe and Otaka, 2006) consists of 46928 tetrahedral cells in a fully three-dimensional computation domain. The details of the sub-models used for flow, heat and mass transfer, the radiation model and the solver settings are the same as that used for the first model. The reactor vessel is cylindrical in shape and is 6m long with a diameter of 0.3m in the combustor region of the gasifier, and a throat diameter of 0.15m. The redactor has the same diameter as the combustor.

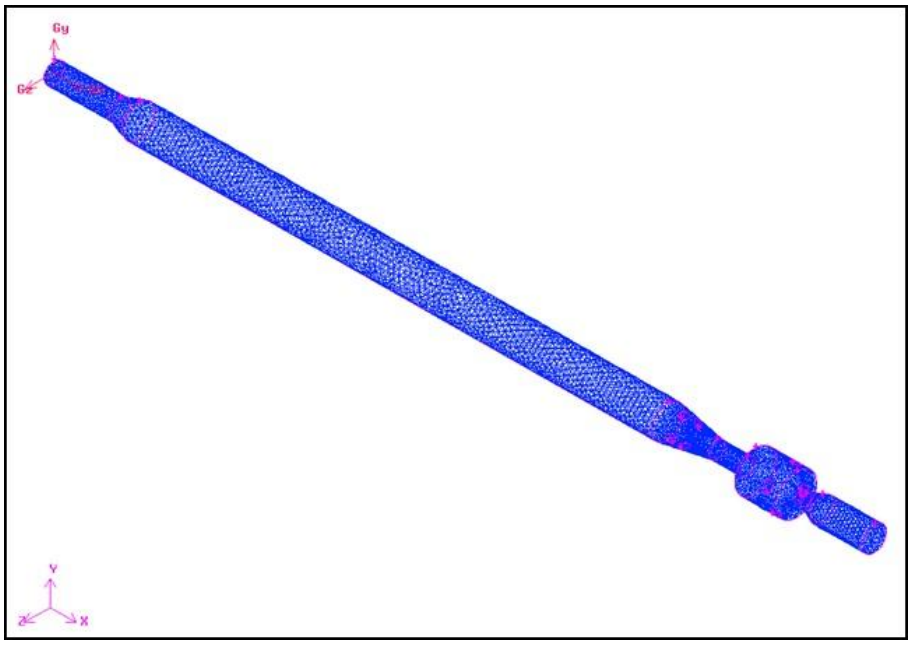

Figure 3.26: Computational mesh for the entrained-flow coal gasifer.

The mesh in Figure 3.26 represents the computational domain for a 2T/day research/lab-scale gasifier consisting of 46928 tetrahedral elements. The design of the gasifier is similar to that in the Chen et al (2000) study with a similar arrangement of inlets and outlet and combustor, diffuser and redactor regions. Two types of coal from Watanabe and Otaka (2006), that is, coal M and coal T have been considered for this study. Coal M is an Australian black coal while coal T is a Japanese black coal. The proximate and ultimate analyses for the two coals are given in the Tables 3.8, 3.9, 3.10 and 3.11 below.

Coal M:

Table 3.8. Proximate analysis (wt %) (wt%)

Component	% by weight
Moisture	4.2
Fixed Carbon	56.2
Volatile Matter	30.9
Ash	8.7

Table 3.9. Ultimate analysis

Element	% by weight
Carbon	76.3
Hydrogen	5.31
Nitrogen	1.54
Oxygen	7.31
Sulfur	0.46

Coal T:

Table 3.10. Proximate analysis (wt %) analysis (wt%)

Component	% by weight
Moisture	5.3
Fixed Carbon	35.8
Volatile Matter	46.8
Ash	12.1

Table 3.11. Ultimate

Element	% by weight
Carbon	68.2
Hydrogen	5.71
Nitrogen	0.99
Oxygen	12.26
Sulfur	0.19

The stoichiometric coefficient values for the volatiles of coal M and coal T are given in Table 3.12 and Table 3.13, respectively.

Table 3.12: Stoichiometric coefficient values for coal M.

Parameter	Value
m11	1.366
m12	4.89
m13	0.422
m14	0.102
m15	0.013

Table 3.13: Stoichiometric coefficient values for coal T.

Parameter	Value
m11	1.53
m12	3.42
m13	0.456
m14	0.042
m15	0.003

Two different feed cases each have been considered for the two coals – M and T, making it four cases in total. The naming convention for the different cases is adapted from Watanabe and Otaka (2006). The operating pressure considered for the gasifier is 2.0 MPa. The feed rates for the different cases are given below in Table 3.14.

Table 3.14. Coal and air feed rates (kg/s)

Gasifier feed	M-1 (kg/hr)	M-3 (kg/hr)	T-1 (kg/hr)	T-3 (kg/hr)
Combustor coal	40.7	40.6	50.1	50.7
Reductor coal	60.3	58.3	52.2	50.5
Recycled char	38.1	34.8	33.6	7.7
Combustor air	391.7	436.6	342.0	371.8
Reductor air	66.96	66.49	61.9	66.3

The injection velocity for the coal particles is 3m/s. A Rosin-Rammler size distribution is used for the coal particles as in the first model. The parameters used for the Rosin-Rammler distribution are: minimum diameter = 4μm, maximum diameter = 150μm, mean diameter = 40μm, spread parameter = 1.2, number of diameters = 6, total number of coal particle packets injected = 20736.

Again, it was observed that the use of fixed wall temperatures in different sections of the gasifier provides better agreement with experimental data than the use of adiabatic conditions at the walls. The fixed wall temperatures employed are 1897K at the combustor region, 1300K at the diffuser region and 1300K at the reductor region of the gasifier.

3.4.2 Results and Discussion

Case M-1

The first case from Watanabe and Otaka (2006) is considered first for this study. The results obtained for the two chemical reaction kinetics schemes are

compared for this case, which in turn are evaluated against the experimental data and simulation results provided by Watanabe and Otaka (2006). A similar comparison is made for three other cases, M-3, T-1 and T-3, and the results summarized and discussed for the two chemical reaction kinetics schemes.

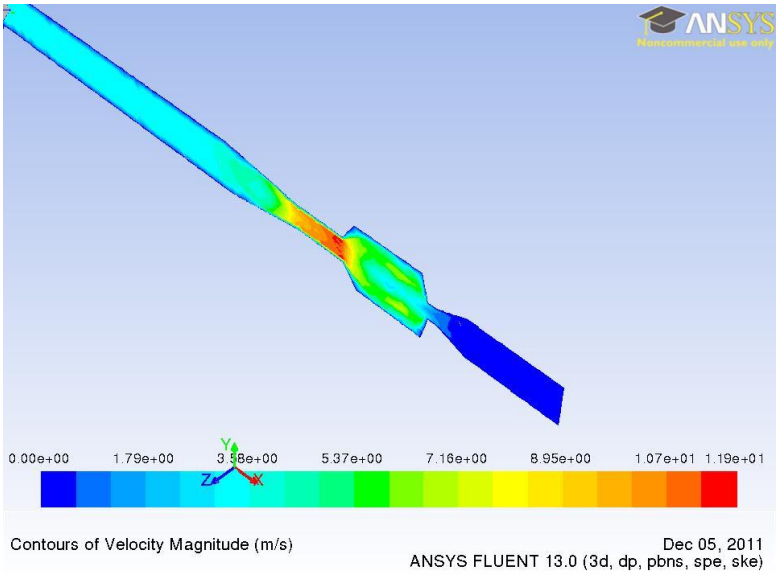

Figure 3.27: Velocity contour profile – Case M1 and Scheme 1.

As anticipated and seen in Figure 3.27, the peak velocity occurs in the region where the gasifier section expands as we move from the combustor to the reductor, which in effect, is a nozzle-type section of the gasifier. The velocity magnitude of the expanding gases (after combustion) in this section exceeds 10m/s.

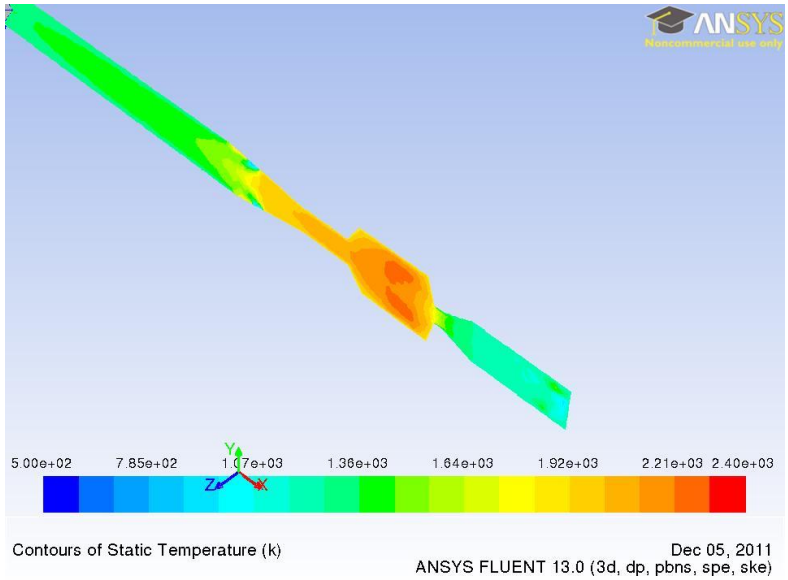

Figure 3.28: Temperature contour profile – Case M1 and Scheme 1.

From Figure 3.28 it is observed that the highest temperatures within the gasifier are seen between the combustor and the reductor in a region close to the combustor inlets. With the first chemical reaction kinetics scheme, it is observed that the maximum temperature is about 2308K, and the minimum about 754K. Since the velocity contours are similar in all the cases (for both the chemical kinetics schemes) considered in this study, henceforth only the temperature contours will be displayed for the different cases and chemical reaction kinetics schemes.

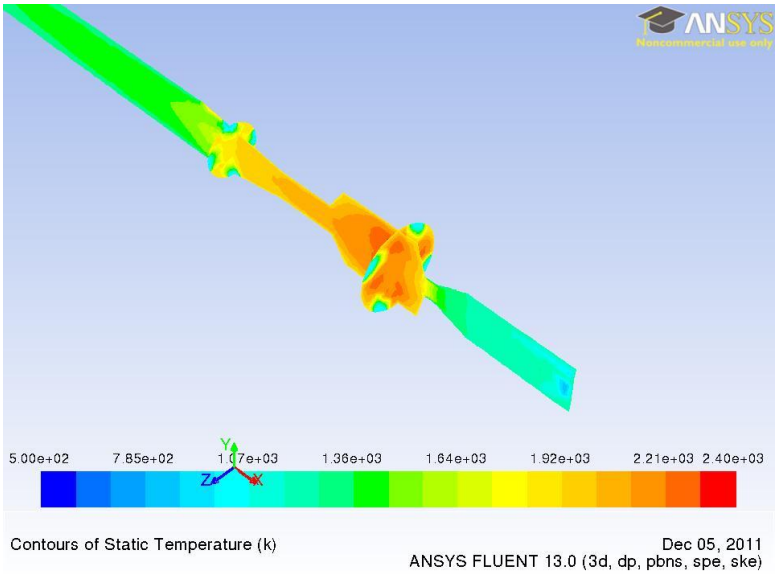

Figure 3.29: Temperature contour profile – Case M1 and Scheme 2.

The location of the peak temperature is similar to that obtained with the first scheme as is seen in Figure 3.29. The spread in the temperatures obtained with the second scheme is higher than for the first, with a higher maximum temperature as well. The peak temperature within the gasifier is around 2329K with the lowest temperature being 739K.

From Figure 3.30 it is seen that the temperature values obtained with the two different schemes within the gasifier along its axis show excellent agreement with the experimental data with the correct temperature trend being captured.

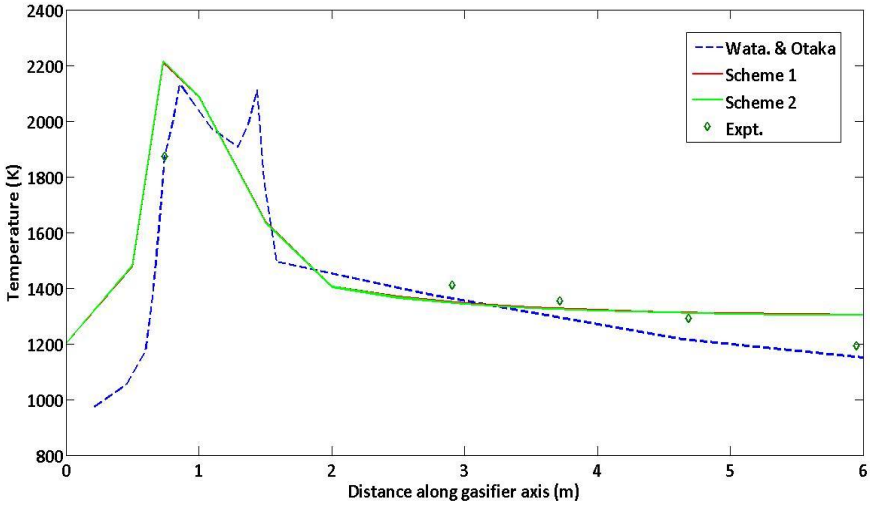

Figure 3.30: Temperature along gasifier axis – Case M1.

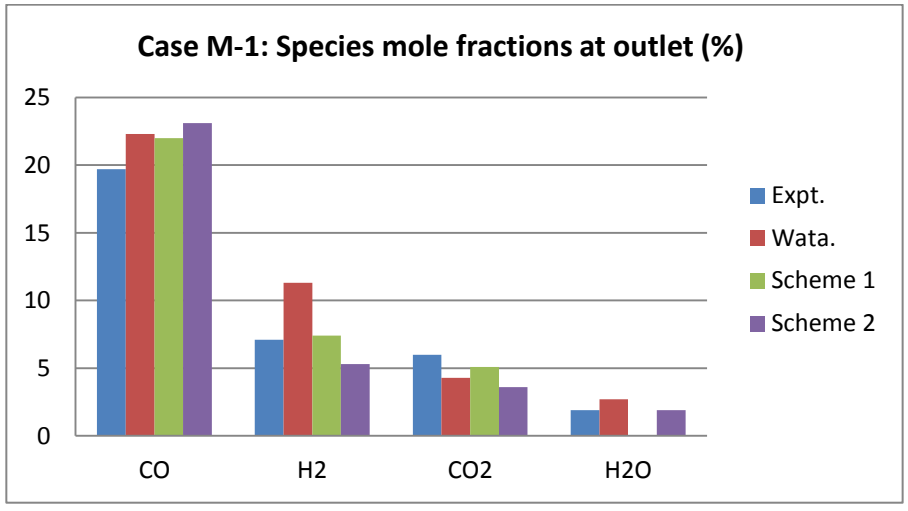

Figure 3.31: Gasifier outlet species mole fractions – Case M1.

Figure 3.31 illustrates that the agreement of experimental data with the results obtained with scheme 1 are very good, with the exception of the mole fraction for water vapor which it fails to predict. It will be observed that the experience with the mole fraction of water vapor is a recurring theme for scheme 1 with all the cases. The agreement with scheme 2 is also good, especially for water vapor. However, for all other species, the agreement with scheme 1 is better than with scheme 2 and the results of Watanabe and Otaka (2006).

Case M-3

As mentioned earlier, the exercise with case M-1 is repeated for all the other cases with the omission of the velocity magnitude contour plot.

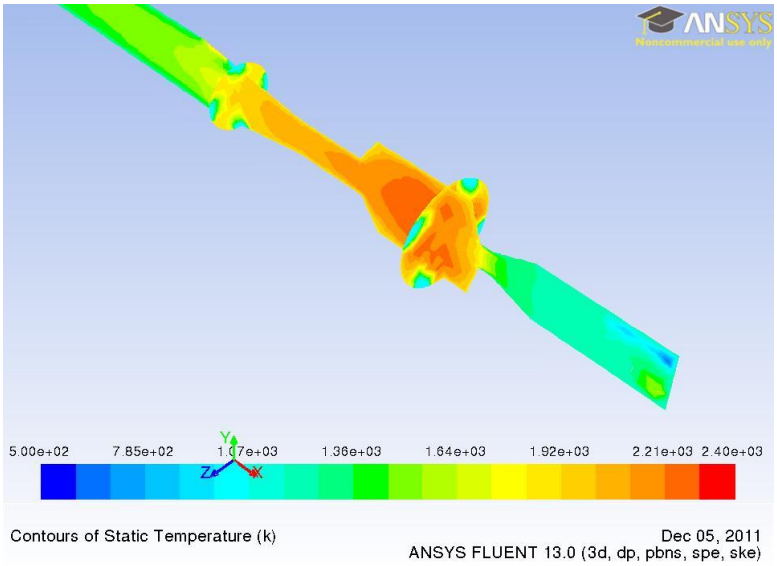

Figure 3.32: Temperature contour profile – Case M3 and Scheme 1.

As observed for case M-1, from the Figure 3.32 it is seen that the peak temperature is seen close to the combustor inlets and directly above them, that is between the combustor and reductor regions of the gasifier. For this case, with the first chemical kinetics scheme implemented, a peak temperature of 2329K and a minimum of 572K is observed within the gasifier. As compared to the case M-1, the oxygen to coal ratio is higher in the M-3 case, and hence the peak observed temperature is also higher.

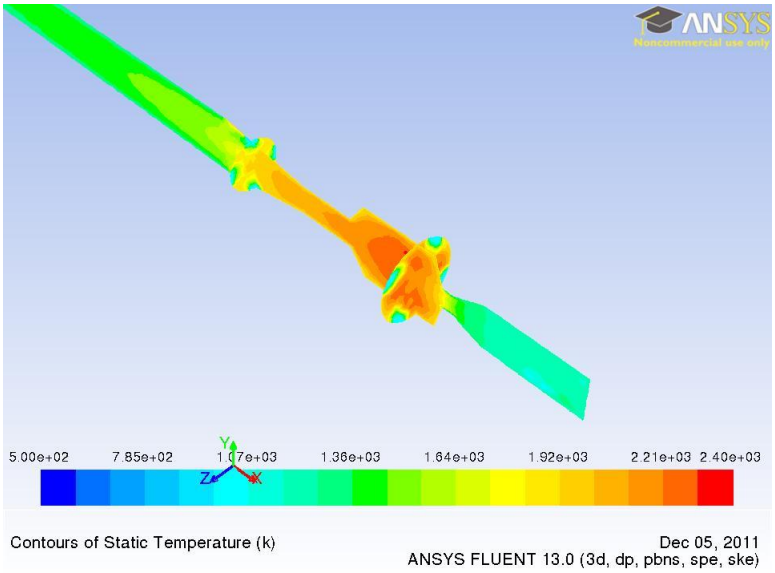

Figure 3.33: Temperature contour profile – Case M3 and Scheme 2.

A similar temperature distribution is observed in Figure 3.33 with the scheme 2 as seen with scheme 1, with a slight difference in peak temperature with the higher value obtained with scheme 2. The maximum temperature observed is then 2341K and the minimum 887K.

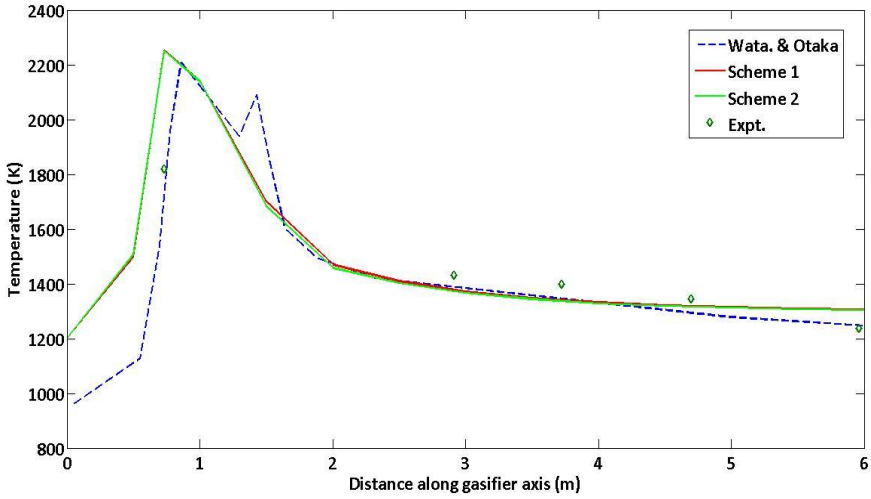

Figure 3.34: Temperature along gasifier axis – Case M3.

As with the case M-1, from Figure 3.34 it is seen that the temperature values obtained with the two different schemes within the gasifier along its axis show good agreement with the experimental data with the correct temperature trend being captured.

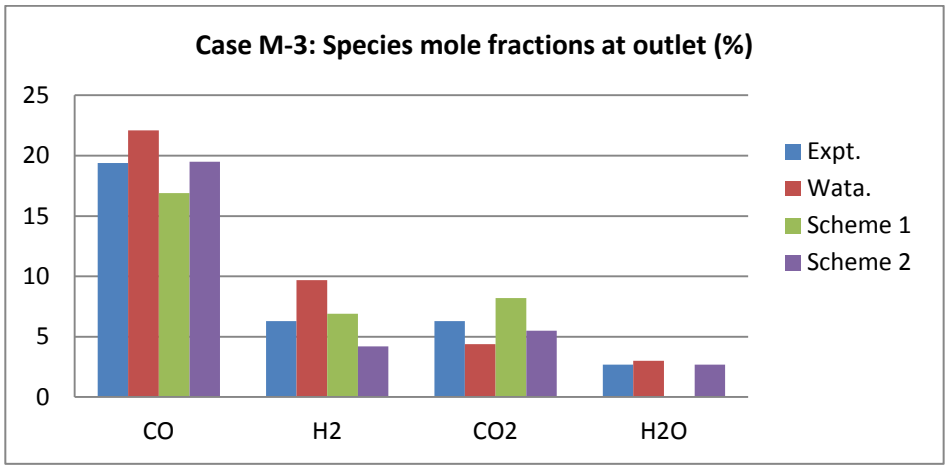

Figure 3.35: Gasifier outlet species mole fractions – Case M3.

Figure 3.35 illustrates that the agreement of experimental data with the results obtained with scheme 1 are good, with the exception of the mole fraction for water vapor. The agreement with scheme 2 is excellent, with the model offering the best predictions with the exception of the mole fraction for hydrogen. With the case M-3 it is seen that scheme 2 outperforms scheme 1 as well as the predictions of Watanabe and Otaka (2006).

Case T-1

As was seen in the earlier cases, from the Figure 3.36 it is apparent that the peak temperature within the gasifier occurs close to the combustor inlets, in the region that can be thought of as a combustion region (or zone) for the gasifier.

For this case, with the first chemical kinetics scheme implemented, a peak temperature of 2246K and a minimum of 875K is observed within the gasifier.

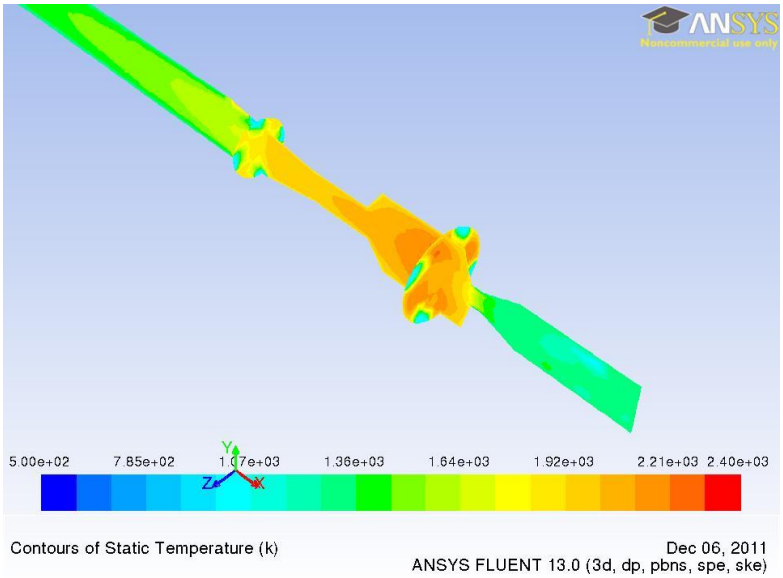

Figure 3.36: Temperature contour profile – Case T1 and Scheme 1.

A temperature distribution similar to scheme 1 is observed with the scheme 2 as seen in Figure 3.37, with a small difference in peak temperature with the higher value obtained with scheme 2. The maximum temperature within the gasifier is estimated as 2257K and the minimum 654K.

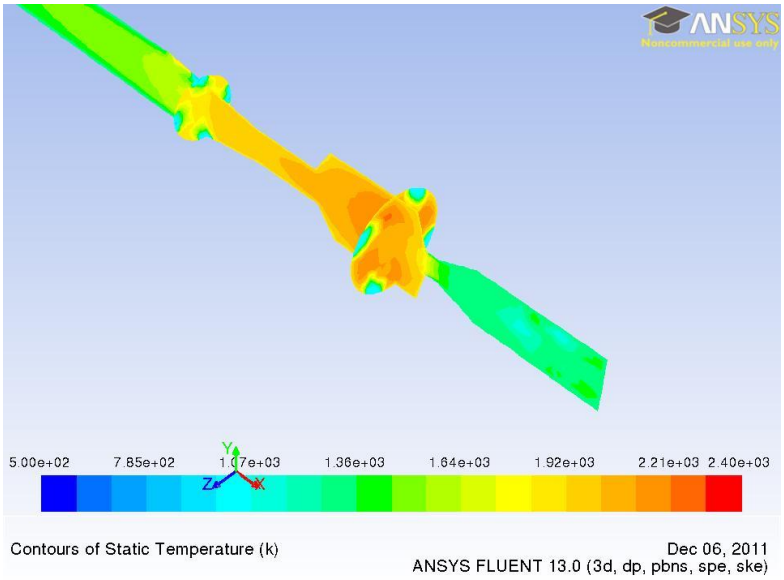

Figure 3.37: Temperature contour profile – Case T1 and Scheme 2.

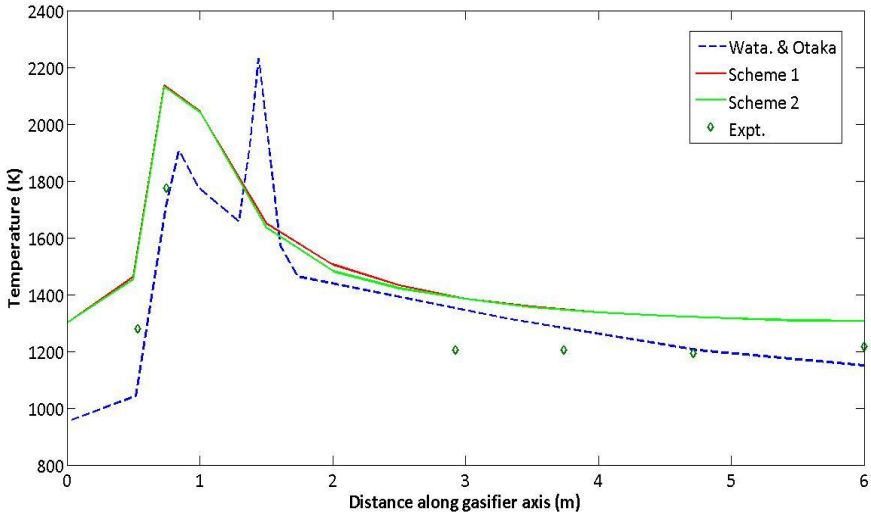

Figure 3.38: Temperature along gasifier axis – Case T1.

As observed with the earlier two cases, from Figure 3.38 it is seen that the temperature values obtained with the two different schemes within the gasifier along its axis show good agreement with the experimental data with the correct temperature trend being captured. However, in the region very close to the combustor inlets, there is a difference in the temperature predicted by the two schemes and the experimental data since the flow field may not be adequately resolved in that region due to insufficient information (swirl, details of injection velocity, turbulence intensity, etc.).

Figure 3.39 illustrates that the agreement of experimental data with the results obtained with scheme 1 are good, with the exception of the mole fraction for water vapor. The agreement with scheme 2 is also good, but in this case it is seen that the predictions of Watanabe and Otaka (2006) offer the closest agreement, with the exception being the mole fraction of hydrogen for which scheme 2 offers the best result.

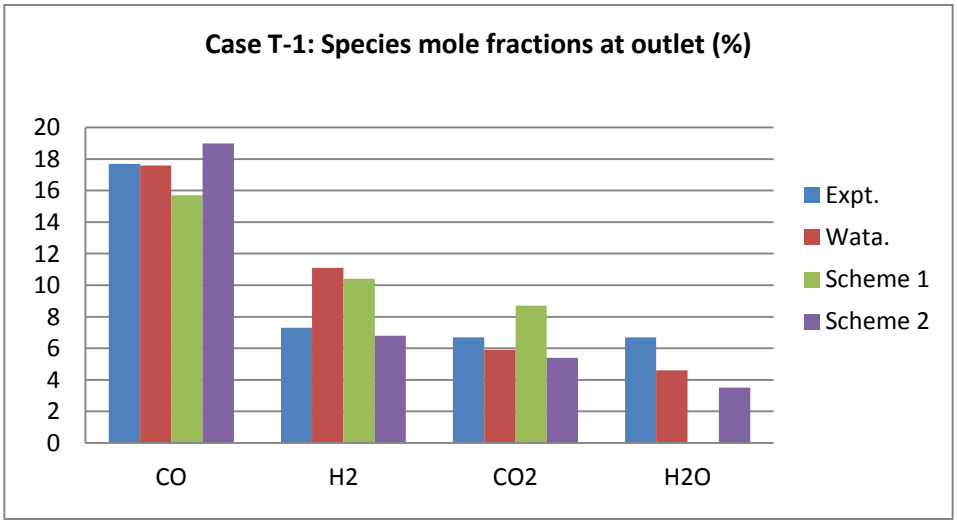

Figure 3.39: Gasifier outlet species mole fractions – Case T1.

Case T-3

As was seen in the earlier, from the Figure 3.40 it is clear that the peak temperature within the gasifier occurs in the combustor region. For this case, with the first chemical kinetics scheme implemented, a peak temperature of 2573K and a minimum of 483K is observed within the gasifier. This peak temperature is unusually high, and this case with scheme 1 needs to be investigated further.

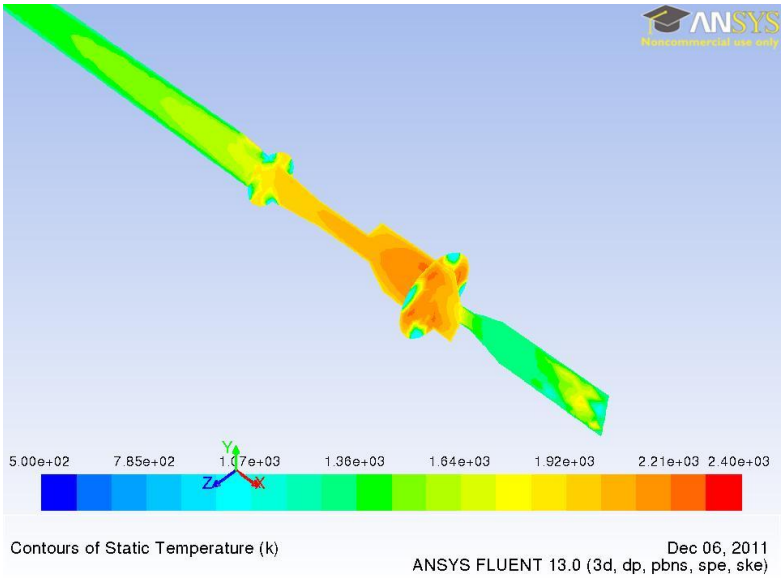

Figure 3.40: Temperature contour profile – Case T3 and Scheme 1.

A temperature distribution similar to scheme 1 is observed with the scheme 2 as seen in Figure 3.41, with a small difference in peak temperature which in this case is unusually low. This could be attributed to the anomalously high peak temperature observed with scheme 1 for the T-3 case. The maximum temperature within the gasifier for scheme 2 is estimated as 2374K and the minimum 656K. The higher temperatures observed with the case T-3 as compared to T-1 can again be explained using the reasoning of higher oxygen to coal feed ratio.

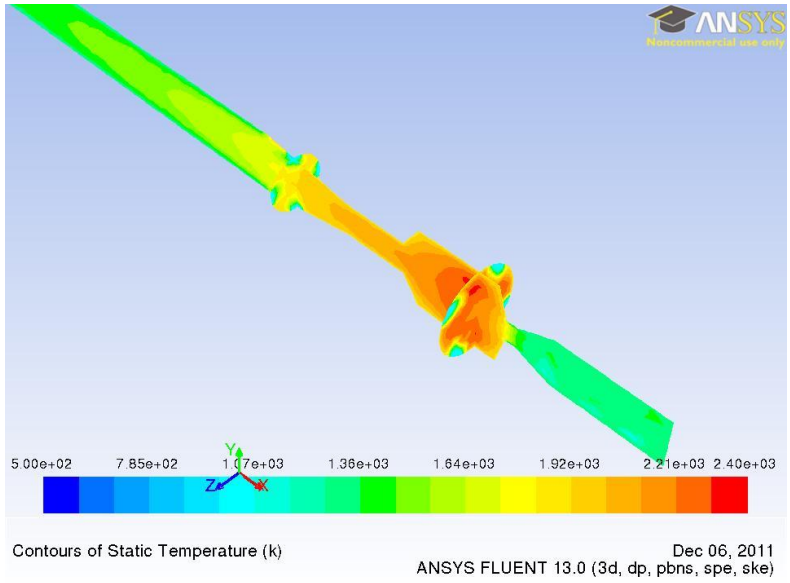

Figure 3.41: Temperature contour profile – Case T3 and Scheme 2.

As observed with the earlier two cases, from Figure 3.42 it is seen that the temperature values obtained with the two different schemes within the gasifier

along its axis show good agreement with the experimental data with the correct temperature trend being captured. Again, the difference between predicted and observed temperatures close to the combustor can be explained with the same reasons given for the T-1 case. In all four cases, the temperature "fall-off" far away from the combustor, with distance from the combustion region is more rapid than the predictions from the two schemes would suggest. This effect might be captured if additional heat loss through the walls is accounted for in the model.

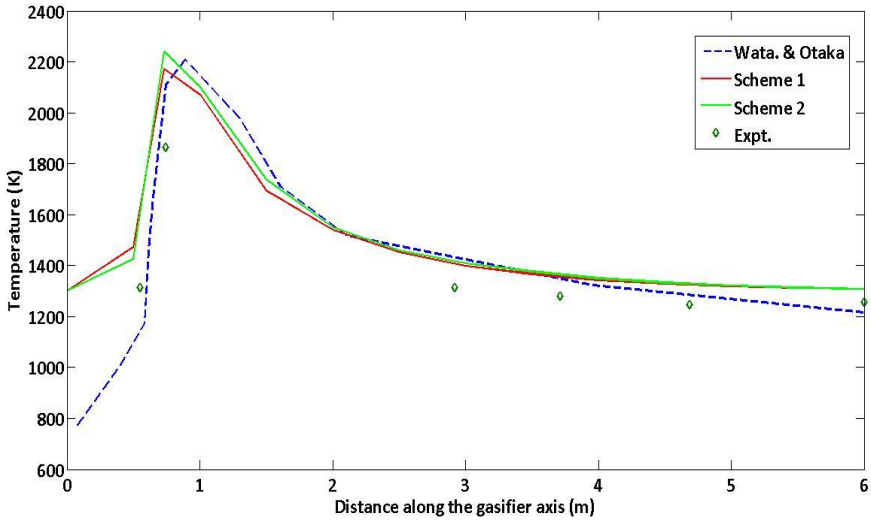

Figure 3.42: Temperature along gasifier axis – Case T3.

Figure 3.43 illustrates that the agreement of experimental data with the results obtained with scheme 1 are good, with the exception of the mole fraction for

water vapor. The agreement with scheme 2 is very good in this case, but so also are the predictions of Watanabe and Otaka (2006). It is a toss-up between scheme 2 and the Watanabe and Otaka (2006) predictions as to which offer the more acceptable results.

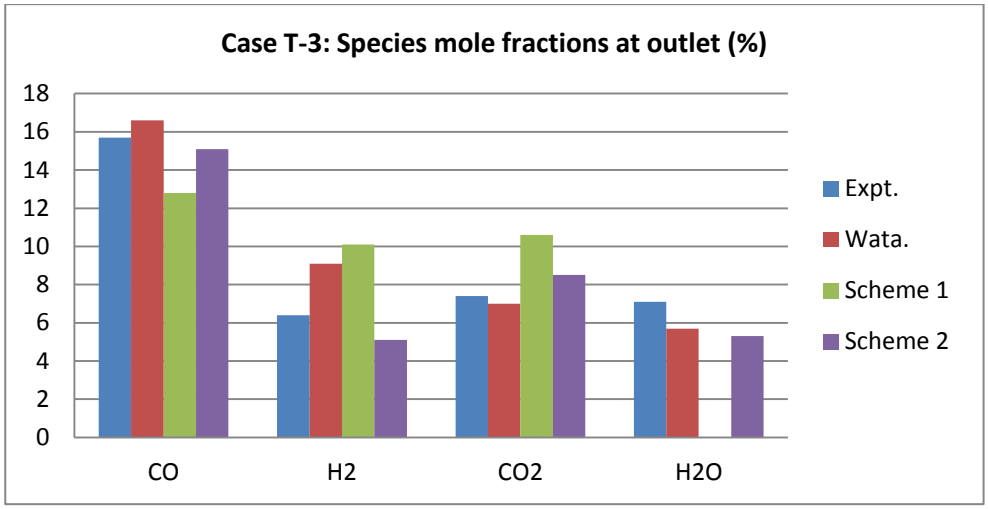

Figure 3.43: Gasifier outlet species mole fractions – Case T3.

Another observation that can be made is that the mole fraction percentage of carbon dioxide is higher in the case of T-3 as compared to T-1 (a similar comparison can be made between M-3 and M-1), and the mole fraction percentage of carbon monoxide lower in the product gas. This is due to the higher oxygen to coal feed ratio in the case of T-3 as compared to T-1 (and M-3 as compared to M-1). Furthermore, this observation can also be made in the

case of hydrogen and water vapor with hydrogen taking the place of carbon monoxide and water vapor that of carbon dioxide in the earlier reasoning given.

3.4.3 Concluding Remarks

For the model described by Watanabe and Otaka (2006), looking at the four cases considered in this study (M-1, M-3, T-1 and T-3), the argument for selection of a particular scheme/model is not that straightforward. For the species mole fractions of the product syngas measured at the gasifier outlet, it is seen that scheme 1 offers the best estimate for case M-1, scheme 2 for M-3, Watanabe and Otaka (2006) for T-1, and both scheme 2 and Watanabe and Otaka (2006) for the T-3 case. Furthermore, all the schemes seem to provide a good estimate for temperature along the gasifier axis, except very close to the combustor inlets. The reason for the difference between observed and predicted values has already been discussed earlier, and this issue needs to be investigated further.

4. HEAVY OIL GASIFICATION

This work focuses on CFD modeling of a lab-scale entrained-flow heavy oil gasifier. The CFD predictions are compared with relevant experimental data to validate how well the model captures the physical and chemical processes taking place within the gasifier.

4.1 Lab-scale Heavy Oil Gasifier

Watanabe et al. (2002) and Ashizawa et al. (2005) performed studies of heavy oil gasification using Orimulsion coke as feedstock for different oxygen ratios in a 2.4t/d lab-scale entrained flow gasifier. The present CFD predictions are compared with their experimental data.

4.1.1 Gasifier Design

The gasifier illustrated in Figure 4.1 is cylindrical with a length of 3m and a diameter of 0.3m. The inlet diameter is 0.075m, and the outlet diameter is 0.15m.

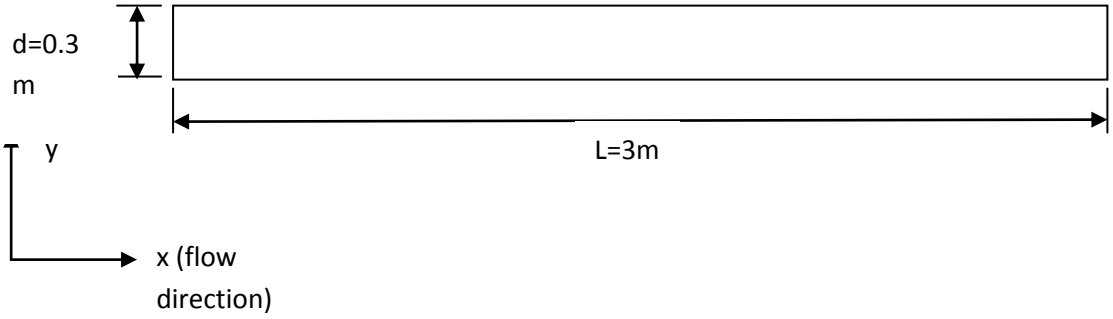

Figure 4.1: Heavy oil entrained-flow gasifier.

The heavy oil gasification is investigated for four different oxygen ratios of 0.36, 0.38, 0.39 and 0.40. The oxygen ratio (λ) is defined as:

$$\lambda = \frac{\text{Oxygen feed rate for the gasifier (kg/hr)}}{\text{Stoichiometric oxygen for gasifier feed (kg/hr)}}$$

The corresponding heavy oil and oxygen feed rates are listed in Table 4.1.

Table 4.1: Gasifier feed rates for different oxygen ratios.

Case	Oxygen ratio	Orimulsion feed rate	Oxygen feed rate	Reference
	[-]	[kg/h]	[kg/h]	
Case 1	0.36	85	69	Watanabe et al. (2002)
Case 2	0.38	85	73	Watanabe et al. (2002)
Case 3	0.39	85	75	Ashizawa et al. (2005)
Case 4	0.40	85	77	Watanabe et al. (2002)

The reactor walls are assumed to be adiabatic no-slip walls.

The oil droplets were assumed to fit a Rosin-Rammler size distribution with a minimum size of 4μm and a maximum of 150, with an average of 40μm. The spread parameter was 1.2 and 10 discrete particle sizes were considered. The heavy oil feed rate is 0.0278kg/s and the oxygen feed rate corresponds to an oxygen ratio of 0.39. The operating pressure used in this model is 1.9MPa.

4.1.2 Modeling Details

The discrete phase method in ANSYS FLUENT 13.0 was used for the CFD simulation. The standard k-ε turbulence model was used for the continuous phase, and stochastic tracking was implemented in a steady-state model of the gasifier to simulate particle motion and turbulent dispersion in two dimensions assuming axisymmetric flow. The computational mesh consists of 300 x 200 uniform quadrilateral control volumes. The SIMPLE algorithm was used to implement the pressure-velocity coupling with the second-order upwind spatial discretization scheme and a Green-Gauss cell based gradient technique.

Conductive, convective and radiative heat transfer was accounted for between the gases, droplets and reactor walls. The scattering property of the droplets due to radiation is assumed to be isotropic and the standard P1 model was used for the purpose of modeling radiative heat transfer. This model is based on the expansion of radiation intensity into an orthogonal series of spherical

harmonics. The weighted-sum-of-gray-gases-model (wsggm) was used to calculate the absorption coefficient of the gas phase.

4.1.3 Results and Discussion

The gasification is run with chemical kinetics scheme listed in Table 2.3 comprising the heterogeneous reaction rates from Watanabe et al. (2002) and the gas-phase reaction rates of Jones & Lindstedt (1988) and Maki & Miura (1997).

Stoichiometric coefficients defining the devolatilization and volatile oxidation reactions are given in Table 4.2. The gasifier is run under oxygen-lean conditions.

Table 4.2: Heavy oil stoichiometric coefficient values.

Parameter	Value
m11	14.88
m12	27.96
m13	0.072
m14	0.124
m15	0.336

The reactive flow in the gasifier is illustrated by contour plots of the temperature distribution in Figure 4.2 and the velocity distribution in Figure 4.3. The influence of the oxygen ratio is included by plotting the cases with the lowest and highest ratios.

A simple preliminary visual comparison can be made between the predictions of case 1 and case 4, that is the cases with the lowest ($\lambda = 0.36$) and highest oxygen ratio ($\lambda = 0.4$), respectively. From Figure 4.2 it is clear that the maximum temperature observed in case 4 is much higher than in case 1. This follows from the fact that a higher oxygen ratio would mean a greater degree of partial oxidation of the feedstock, resulting in a higher amount of CO_2 in the product gas.

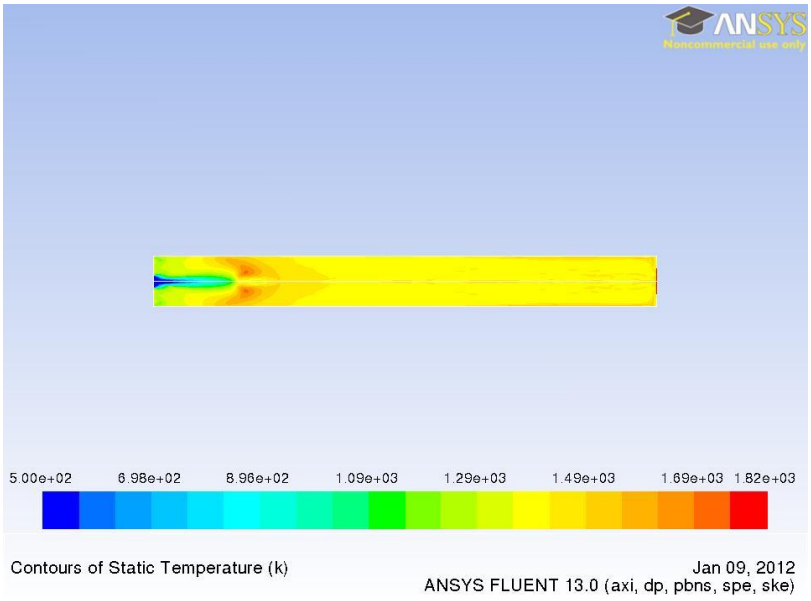

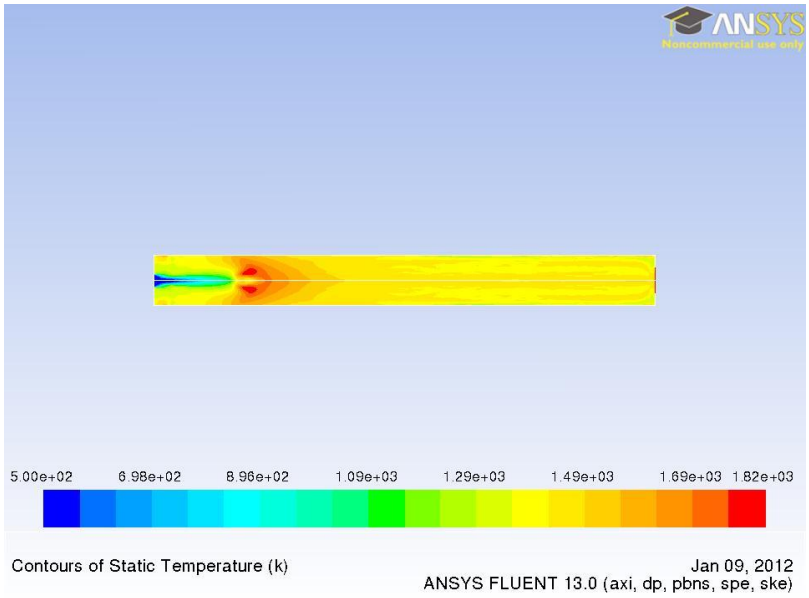

Figure 4.2: Temperature contour plot. Influence of oxygen ratio: λ = 0.36 (top) and λ = 0.40 (bottom).

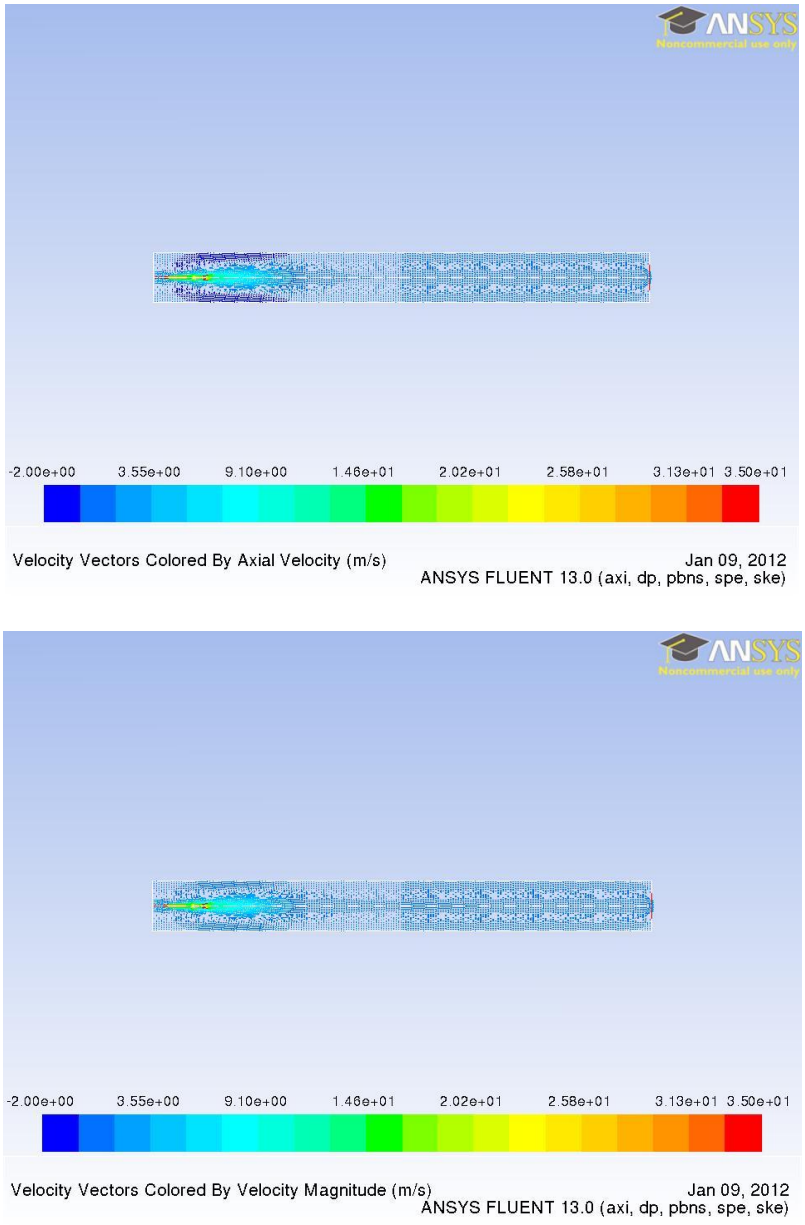

Figure 4.3: Axial velocity vector plot. Influence of oxygen ratio: λ = 0.36 (top) and λ = 0.40 (bottom).

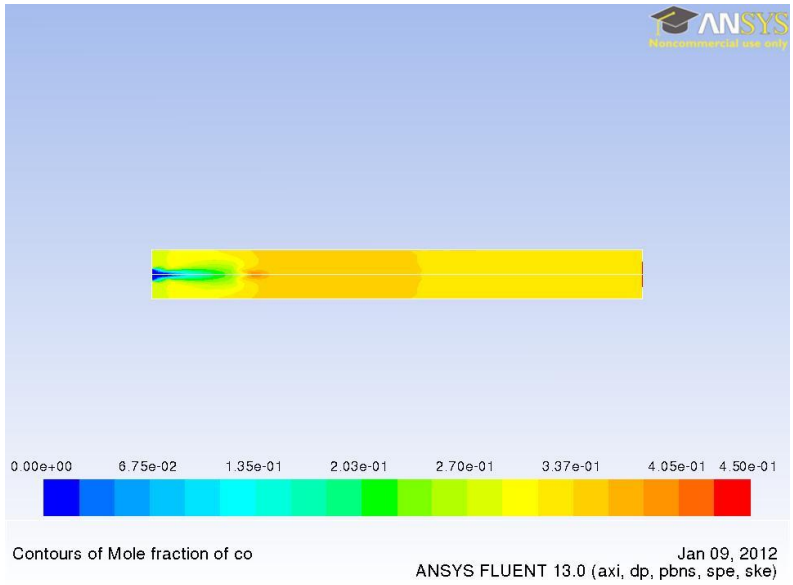

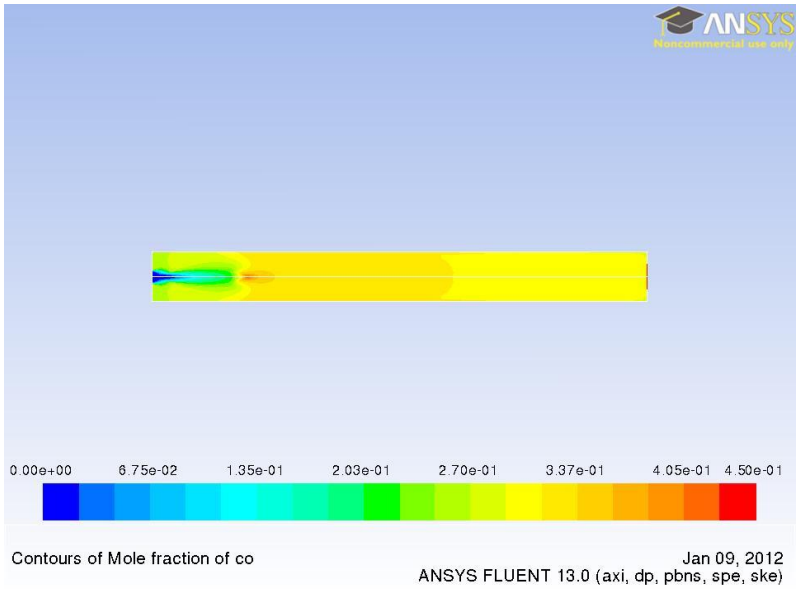

Figure 4.4: CO mole fraction contour plot. Influence of oxygen ratio: $\lambda = 0.36$ (top) and $\lambda = 0.40$ (bottom).

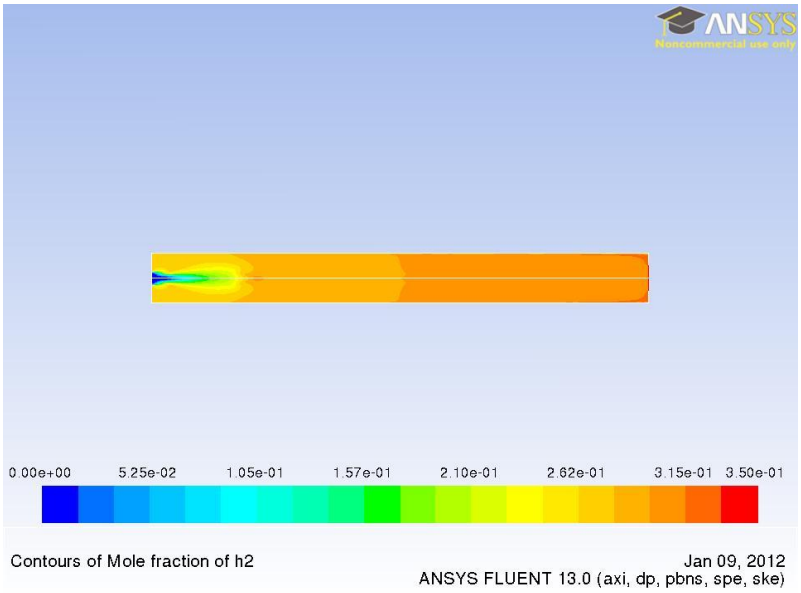

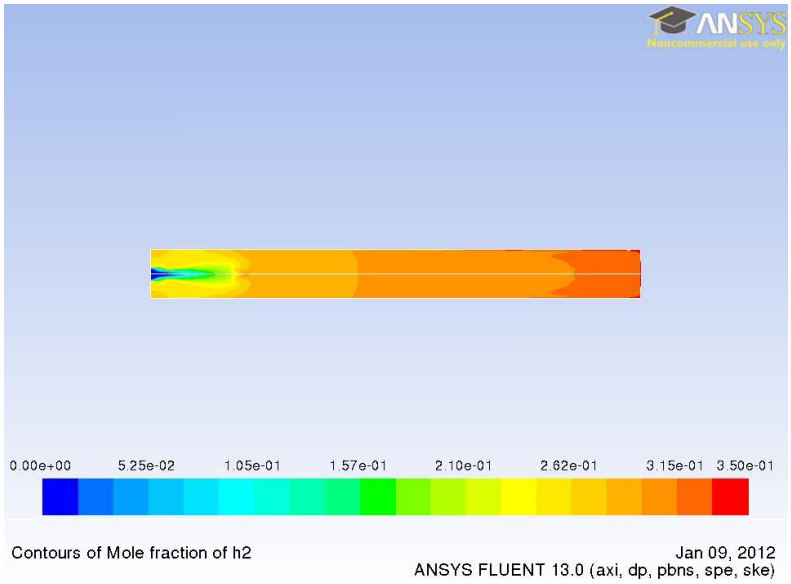

Figure 4.5: H_2 mole fraction contour plot. Influence of oxygen ratio: $\lambda = 0.36$ (top) and $\lambda = 0.40$ (bottom).

The location of this peak temperature corresponds to the combustion zone within the gasifier, and is located about 0.5m – 0.7m downstream of the gasifier inlet. The maximum temperature observed in case 1 is 1702K and 1812K in case 4. About 0.4m – 0.5m from the inlet lies the zone in which devolatilization is most active within the gasifier.

The velocity profiles for the low (case 1) and high oxygen ratio (case 4) cases are similar, with not much of a difference in the velocity fields. However, a stronger recirculation zone is observed at the walls close to the inlet for case 1. This can be observed in Figure 4.3.

From Figure 4.4 it is observed that there is a larger buildup of CO within the gasifier for the low oxygen ratio case as compared to the high oxygen ratio case. It can also be noticed from Figure 4.5 that there is not much of a difference in the amount of H_2 within the gasifier when we compare case 1 and case 4, with case 4 having a marginally higher estimate of hydrogen mole fraction.

The predicted temperature profiles along the gasifier centerline are shown in Figure 4.6 for different oxygen ratios. The agreement with the experimental data of Watanabe et al. (2002) and Ashizawa et al. (2005) is quite good. The cooling of the hot product gases downstream of the devolatilization and combustion/gasification zones is correctly predicted. Likewise, a higher gasifier temperature with higher oxygen ratios due to a higher amount of oxygen available for gasification and combustion is also correctly predicted. Although experimental data is missing in the inlet and combustion region of the gasifier, the peak temperature in the devolatilization and combustion/gasification zones

appears to be underpredicted. The gasifier exit temperature is slightly overpredicted. The maximum error is less than 4%, with the exception of case 3 where the maximum error is almost 14%.

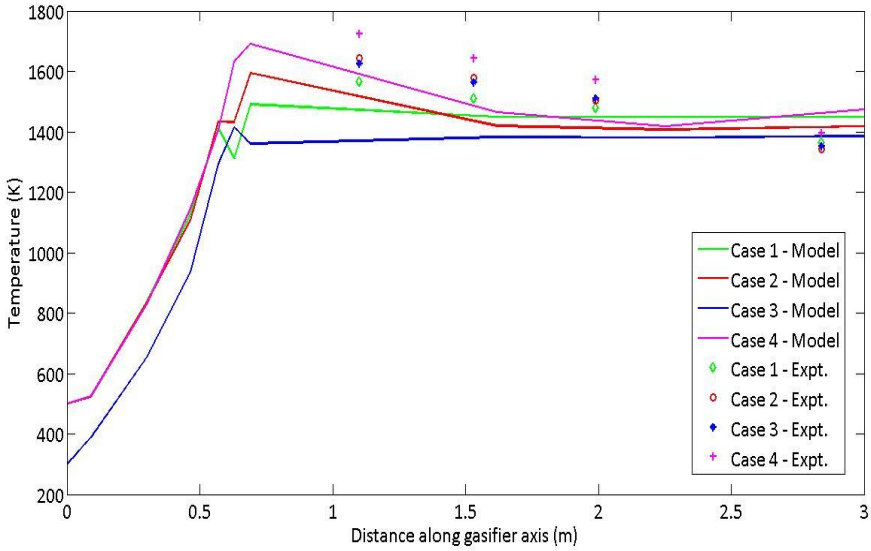

Figure 4.6: Axial temperature distribution for different oxygen ratios. Experimental data from Watanabe et al. (2002) and Ashizawa et al. (2005).

The CFD predictions perform very well in predicting the gasifier outlet measurement as indicated in Figure 4.7. The predicted mole fraction of carbon monoxide CO and hydrogen H_2 which are the two major species are underpredicted with less than 9% of the measured value. The predicted mole fraction of carbon monoxide CO_2 and water vapour H_2O which are the two minor species are, however, overpredicted with as much as 53% of the measured value. The decreasing mole fraction of carbon monoxide CO and the increasing mole fraction of carbon dioxide CO_2 with increasing oxygen ratio are

correctly predicted. The trends for the mole fraction of hydrogen H_2 and water vapour H_2O are predicted opposite the measurements. It is observed that the overall error percentages are the lowest for case 4, that is, when the oxygen ratio is the highest ($\lambda = 0.4$).

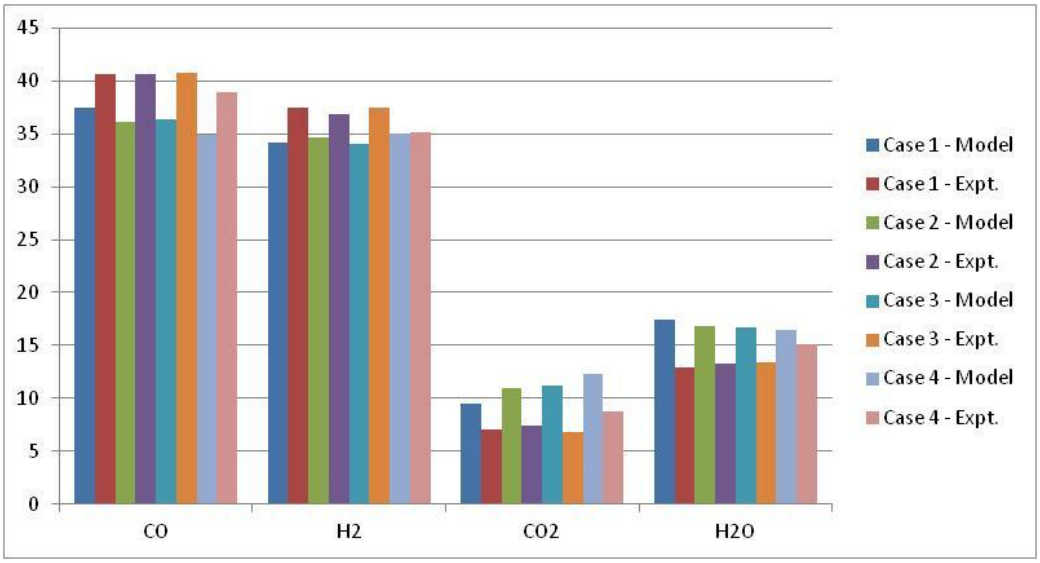

Figure 4.7: Species mole fraction % at gasifier outlet for different oxygen ratios.

A comparison of predicted and measured mole fraction of carbon monoxide along the gasifier centerline is shown in Figure 4.8 for different oxygen ratios. Both the variations with axial distance and oxygen ratio are very well captured. The absolute error is never exceeding 10%. As observed with the gasifier outlet data, the model consistently underestimates the carbon monoxide mole fraction along the gasifier axis.

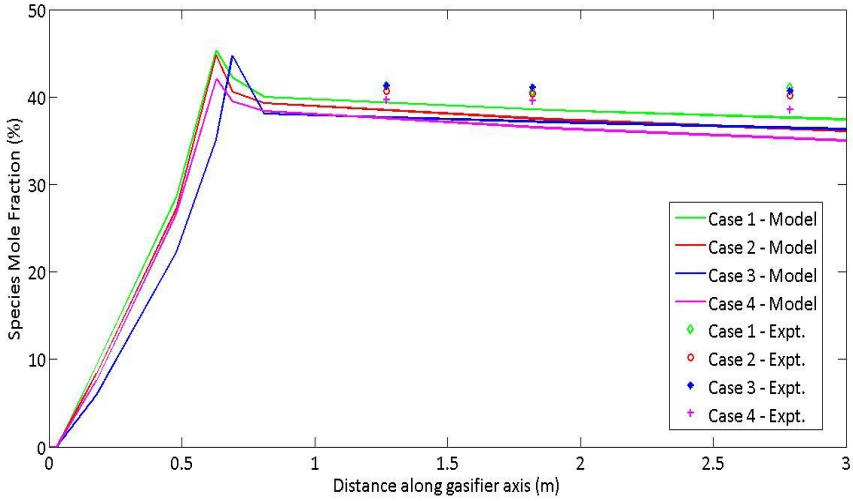

Figure 4.8: Axial CO species mole fraction % for different oxygen ratios.

A comparison of predicted and measured mole fraction of hydrogen H_2 along the gasifier centerline is shown in Figure 4.9 for different oxygen ratios. The variation with axial distance is again very well captured. Unlike the measurements, there is almost no influence of the oxygen ratio. The absolute error being the largest for the smallest oxygen ratio is of the order of 15%.

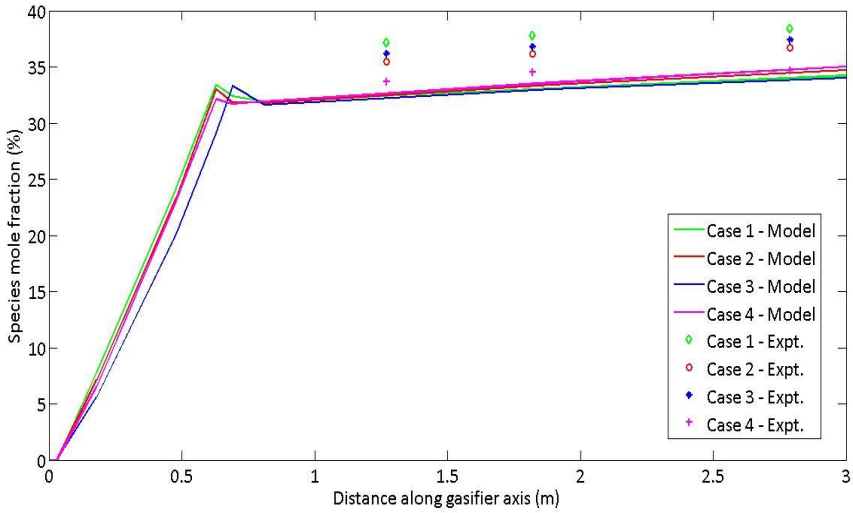

Figure 4.9: Axial H_2 species mole fraction % for different oxygen ratios.

Only the major species axial mole fraction distributions have been compared with experimental data, which are the species mole fractions of carbon monoxide and hydrogen. A similar argument or case can be made for carbon dioxide and water vapor, with similarities in the axial trends (and values) of the experiment and model predicitions for carbon dioxide, with slight differences for water vapor (as was observed for hydrogen).

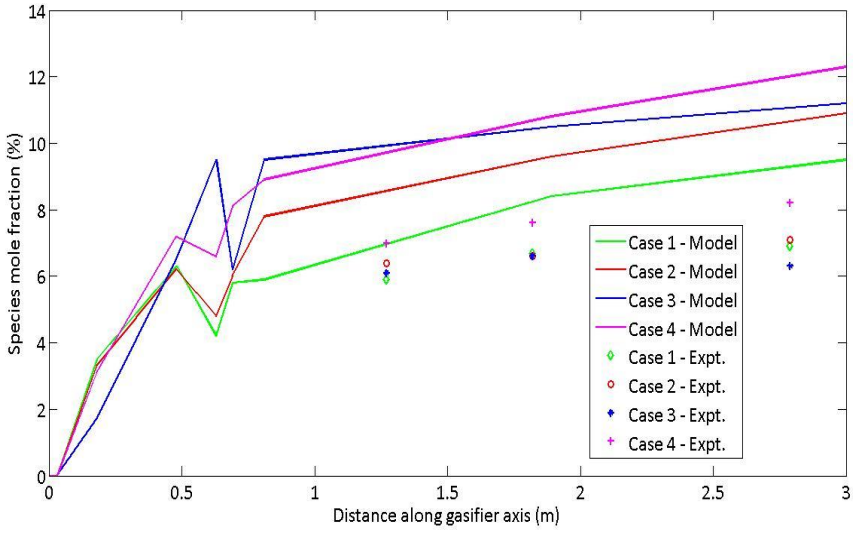

Figure 4.10: Axial CO_2 species mole fraction % for different oxygen ratios.

From Figure 4.10 it is seen that the model predicts the axial trends for CO_2 mole fraction for the different oxygen ratio cases very well, with perhaps the exception of case 3. Again, due to lack of experimental data in the combustion zone of the gasifier, it is difficult to tell whether the model predicts the correct species mole fractions in that region. However, further downstream it is seen that there is good agreement of the experimental and predicted values, with there being a larger difference between experimental and predicted values near the outlet. This model over-estimates the mole fraction of CO_2 within the gasifier, with errors ranging between 18% and 44%.

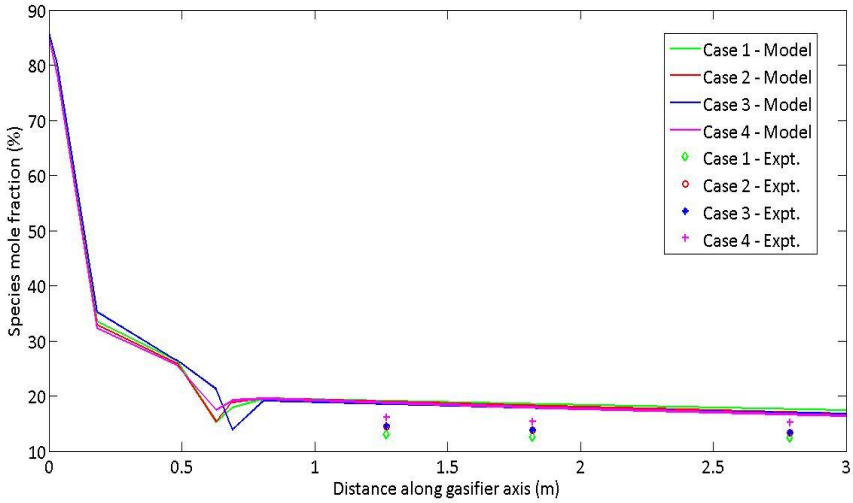

Figure 4.11: Axial H_2O species mole fraction % for different oxygen ratios.

As seen with CO_2, it is seen from Figure 4.11, that the model slightly over-estimates the water vapor mole fraction within the gasifier. The trend is again captured very well, and for this species, holds true in all the cases. The errors in predicted as compared to measured values vary anywhere between 24% and 46%, with the best results being observed for case 4.

4.1.4 Concluding Remarks

The CFD model for the gasification of heavy oil has now been validated for four different oxygen ratios against the experiments by Watanabe et al (2002) and Ashizawa et al. (2005). The accurate chemical composition of the heavy oil (Orimulsion^{TM}) was obtained from its proximate and ultimate analysis, and

more detailed volatiles chemistry has been considered as compared to previous studies in literature.

From the predictions observed earlier, it is clear that the model captures very well the axial values and trends for temperature and mole fractions of the major species obtained during the gasification of heavy oil. The error in maximum temperature observed within the gasifier in the combustion zone never exceeds 5% for cases 1, 2 and 4 with the error exceeding 14% for case 3. The model slightly under-predicts the absolute values for the axial species mole fractions of carbon monoxide and hydrogen, while slightly over-predicting the values for carbon dioxide and water vapor.

Further refinement of the model, including (but not limited to) more detailed combustion modeling for the heavy oil, use of more sophisticated turbulence and radiation models, use of the eddy-dissipation concept, etc. might lead to even more accurate results.

5. CONCLUSIONS

In this work, a computational fluid dynamics (CFD) model based on an Euler-Lagrange multiphase flow model known as the discrete phase method (DPM) was developed, which is applicable to dilute flows. This model was then used to describe the different physical and chemical processes occurring within a coal and heavy oil entrained-flow gasifier.

5.1 Coal Gasification

Two different chemical kinetics schemes were proposed for the lab-scale and pilot-scale entrained-flow coal gasifiers. Three studies involving lab-scale coal gasifiers, as described in Soelberg et al (1985), Ajilkumar et al (2009) and Watanabe & Otaka (2006) and one study involving a pilot-scale coal gasifier as described by Chen et al (2000) formed the basis of comparison and a source for experimental data.

One common trend displayed by the model (using both chemical kinetic schemes) in all the coal gasification studies (with the exception of Soelberg et al (1985)) is that it underestimates the carbon monoxide and hydrogen mole fraction values while overestimating the carbon dioxide and water vapour mole fraction values. It is also seen that scheme 2 performs consistently better than scheme 1 in predicting both the temperature and species mole fraction

distributions within the gasifier, and is hence more suitable for use in coal gasification studies.

The first gasifier under study was an oxygen-blown lab-scale coal gasifier as described by Soelberg et al (1985). For this gasifier the mole fraction of the different major species comprising the product syngas had been estimated. It was seen that the model captured the radial trends for the molar fractions of carbon dioxide, carbon monoxide and hydrogen quite well. The absolute values of mole fractions at different radial locations within the gasifier were well-estimated for carbon dioxide, but the model under-predicts the carbon monoxide mole fraction and over-predicts the hydrogen mole fraction.

The next gasifier studied was an idealized lab-scale air-blown gasifier as described in Ajilkumar et al (2009). The two chemical kinetics schemes mentioned earlier were used, and their predictions compared with the numerical estimates of Ajilkumar et al (2009), using the experimental data of Watanabe et al (2006) as the comparison benchmark. From the model predictions, it was observed that scheme 1 incorrectly predicted the temperature distribution along the gasifier axis, while scheme 2 performed the task well. It was also seen that scheme 2 produced more accurate results when investigating the gasifier outlet species mole fractions. The over-prediction of hydrogen and the non-prediction of water vapour were of some concern with scheme 1.

The third gasifier studied was a pilot-scale air-blown coal gasifier (MHI type) as described by Chen et al (2000) and studied experimentally and numerically by them. The estimates produced by the two chemical kinetics schemes for temperature and species mole fraction distributions of the major species

comprising the product syngas were compared with the experimental data and numerical predictions of Chen et al (2000). It was observed that chemical reaction kinetics scheme 2 provided the best estimates; both with respect to the species mole fractions of the product gases as well as the temperature distribution observed along the gasifier axis. Both the schemes exhibited axial trends for temperature and species mole fractions similar to that given in the experimental data of Chen et al (2000).

The last coal gasifier in this study was a lab-scale air-blown gasifier (CRIEPI gasifier) which could be thought of as a scaled-down version of an MHI type gasifier. The gasifier details were as described by Watanabe and Otaka (2006) – considering four of the experimental cases in that work (M-1, M-3, T-1 and T-3). Considering the predictions using the two chemical kinetics schemes and comparing them with the numerical estimates and experimental data from Watanabe et al (2006), it is tough to pick a model as most suitable. However, looking at the species mole fractions of the product syngas measured at the gasifier outlet, it was seen that scheme 1 provided the best estimate for case M-1, scheme 2 for M-3, Watanabe and Otaka (2006) for T-1, and both scheme 2 and Watanabe and Otaka (2006) for the T-3 case. Combining that fact with the axial temperature distribution predictions, a case could be made for scheme 2 to be suitable for use in coal gasification studies.

5.2 Heavy Oil Gasification

The CFD model for the gasification of heavy oil had been validated for four different oxygen ratios against the experiments by Watanabe et al (2002) and Ashizawa et al (2005). The accurate chemical composition of the heavy oil (Orimulsion^{TM}) was obtained from its proximate and ultimate analysis, and more detailed volatiles chemistry had been considered as compared to previous studies in literature. Cases 1, 2 and 4 use the experiments of Watanabe et al (2002) as a comparison basis, while case 3 follows the experiments of Ashizawa et al (2005). The error in maximum temperature observed within the gasifier in the combustion zone never exceeds 5% for cases 1, 2 and 4 with the error exceeding 14% for case 3. More convincing predictions had been obtained for carbon monoxide and hydrogen mole fractions (smaller error %) as compared to carbon dioxide and hydrogen. As has usually been the case, the model overestimated the water vapor and carbon dioxide mole fractions while underestimating the carbon monoxide and hydrogen mole fractions.

5.3 Future Work

Some improvements could be effected on the modeling predictions by using the following methods:

More detailed/comprehensive global reaction chemistry (instead of the reduced mechanisms used), more detailed combustion modeling for coal and heavy oil, and the use of more sophisticated turbulence and radiation models.

REFERENCES

Ajilkumar, A., Sundararajan T. and Shet, U.S.P. (2009). Numerical modeling of a steam-assisted tubular coal gasifier. *International Journal of Thermal Sciences*, **48**, 308-321.

Alam, M.S., Wijayanta, A.T., Nakaso, K., Fukai, J., Norinaga, K. and Hayashi, J. (2010). A reduced mechanism for primary reactions of coal volatiles in a plug flow reactor. *Combustion Theory and Modelling*, **14**(6), 841-853.

Ashizawa, M., Hara, S., Kidoguchi, K. and Inumaru, J. (2005). Gasification characteristics of extra-heavy oil in a research-scale gasifier. *Energy*, **30**, 2194-2205.

Bockelie, M.J., Swensen, D.A., Dension, M.K., Chen, Z., Senior, C.L. and Sarofim, A.F. (2002). A computational workbench environment for virtual simulation of a vision 21 energyplex. *Proceedings of the 2002 International Joint Power Generation Conference*, 979-986.

Bradley, D., Lawes, M., Scott, M.J. and Usta, N. (2001). The Structure of Coal-Air-CH_4 Laminar Flames in a Low-Pressure Burner: CARS Measurements and Modeling Studies. *Combustion and Flame*, **124**, 82-105.

Brown, B.W., Smoot, L.D., Smith, P.J. and Hedman, P.O. (1988). Measurement and Prediction of Entrained-Flow Gasification Processes. *AIChE Journal*, **34**(3), 435-446.

Callaghan, C.A. (2006). Kinetics and Catalysis of the Water-Gas-Shift Reaction: A Microkinetic and Graph Theoretic Approach. *Ph. D. Thesis*, Worcester Polytechnic Institute, U.S.A.

Chen, C., Horio, M. and Kojima, T. (2000). Numerical simulation of entrained flow coal gasifiers. Part I: modeling of coal gasification in an entrained flow gasifier. *Chemical Engineering Science*, **55**, 3861-3874.

Choi, Y.C., Li, X.Y., Park, T.J., Kim, J.H. and Lee, J.G. (2001). Numerical Analysis of the Flow Field inside an Entrained-Flow Gasifier. *Korean Journal of Chemical Engineering*, **18**(3), 376-381.

Chui, E.H., Majeski, A.J., Lu, D.Y., Hughes, R., Gao, H., McCalden, D.J. and Anthony, E.J. (2009). Simulation of Entrained Flow Coal Gasification. *Energy Procedia 1*, 503-509.

Collot, A. (2002). Matching gasifiers to coals. *Profiles*, IEA Clean Coal Centre.

Du, W., Bao, X., Xu, J. and Wei, W. (2006). Computational fluid dynamics (CFD) modeling of spouted bed: Influence of frictional stress, maximum packing limit and coefficient of restitution of particles. *Chemical Engineering Science*, **61**, 4558-4570.

Field, M.A. (1969). Rate of Combustion of Size-Graded Fractions of Char from a Low Rank Coal between 1200K – 2000K. *Combustion and Flame*, **13**, 237-252.

Gera, D., Syamlal, M. and O'Brien, T.J. (2004). Hydrodynamics of particle segregation in fluidized beds. *International Journal of Multiphase Flow*, **30**, 419-428.

Govind, R. and Shah, J. (1984). Modeling and Simulation of an Entrained Flow Coal Gasifier. *AIChE Journal*, **30**(1), 79-92.

Goyal, A. and Gidaspow, D. (1982). Modeling of Entrained Flow Coal Hydropyrolysis Reactors. 1. Mathematical Formulation and Experimental Verification. *Industrial & Engineering Chemistry Process Design and Development*, **21**, 611-624.

Haberman, W.L. and Sayre, R.M. (1958). Motion of rigid and fluid spheres in stationary and moving liquids inside cylindrical tubes. David Taylor Model Basin Report No. 1143.

Hasegawa, T. (2007). Development of gas turbine combustor for each gasified fuel and prospect of high-efficiency generation of various resources.

International Journal of Gas Turbine, Propulsion and Power Systems, **1**(1), 9-21.

Higman, C. and van der Burgt, M. (2008). *Gasification*, 2nd Ed. Elsevier Inc.

Jenkins, S. (2008). Gasification 101. *Gasification Technologies Council Workshop*.

Jones, W.P. and Lindstedt, R.P. (1988). Global Reaction Schemes for Hydrocarbon Combustion. *Combustion and Flame*, **73**, 233-249.

Kobayashi, H., Howard, J.B. and Sarofim, A.F. (1976). *Sixteenth Symposium (International) on Combustion - The Combustion Institute*, 411-425.

Liu, H., Chen, C. and Kojima, T. (2002). Theoretical Simulation of Entrained Flow IGCC Gasifiers: Effect of Mixture Fraction Fluctuation on Reaction Owing to Turbulent Flow. *Energy & Fuels*, **16**, 1280-1286.

Lockwood, F.C., Salooja, A.P. and Syed, S.A. (1980). A prediction method for coal-fired furnaces. *Combustion and Flame*, **38**(C), 1-15.

Magnussen, B.F. (1981). On the Structure of Turbulence and a Generalized Eddy Dissipation Concept for Chemical Reaction in Turbulent Flow. *19th AIAA Aerospace Science Meeting*.

Magnussen, B.F. and Hjertager, B.H. (1976). On Mathematical Models of Turbulent Combustion with Special Emphasis on Soot Formation and Combustion. *Sixteenth Symposium (International) on Combustion - The Combustion Institute*, 719-729.

Mailybaev, A.A., Bruining, J. and Marchesin, D. (2011). Analysis of in situ combustion of oil with pyrolysis and vaporization. *Combustion and Flame*, **158**, 1097-1108.

Maki, T. and Miura, K. (1997). A Simulation Model for the Pyrolysis of Orimulsion. *Energy & Fuels*, **11**, 819-824.

Niksa, S., Liu, G. and Hurt, R.H. (2003). Coal conversion submodels for design applications at elevated pressures. Part I. devolatilization and char oxidation. *Progress in Energy and Combustion Science*, **29**, 425-477.

Phillips, J. (2006). Different Types of Gasifiers and Their Integration with Gas Turbines. *The Gas Turbine Handbook*, NETL.

Ranz, W.E. and Marshall, W.R. Jr. (1952). Evaporation from drops. *Chemical Engineering Progress*, **48**, 141-144.

Rezaiyan, J., Bechtel, T., Weisenfeld, H. and Cheremisinoff, N. (2003). Assessment of the Commercial Potential for Small Gasification Combined Cycle and Fuel Cell Systems - Phase II Final Draft Report. *Prepared for the U.S. Department of Energy*.

Schiller, L. and Naumann, Z. (1935). A drag coefficient correlation. *Z. Ver. Deutsch. Ing.*, **77**, 318.

Shi, S.P., Zitney, S.E., Shahnam, M., Syamlal, M. and Rogers, W.A. (2006). Modelling coal gasification with CFD and discrete phase method. *Journal of the Energy Institute*, **79**(4), 217-221.

Siegel, R. and Howell, J.R. (1992). Thermal Radiation Heat Transfer (3rd Edition), *McGraw Hill*.

Silaen, A. and Wang, T. (2010). Effect of turbulence and devolatilization models on coal gasification simulation in an entrained-flow coal gasifier. *International Journal of Heat and Mass Transfer*, **53**, 2074-2091.

Skodras, G., Kaldis, S.P., Sakellaropoulos, G.P., Sofialidis, D. and Faltsi, O. (2003). Simulation of a molten bath gasifier by using a CFD code. *Fuel*, **82**, 2033-2044.

Smoot, L.D. (1984). Modeling of Coal-Combustion Processes. *Progress in Energy and Combustion Sciences*, **10**, 229-272.

Smoot, L.D. and Brown, B.W. (1987). Controlling mechanisms in gasification of pulverized coal. *Fuel*, **66**, 1249-1256.

Soelberg, N.R., Smoot, L.D. and Hedman, P.O. (1985). Entrained flow gasification of coal – 1. Evaluation of mixing and reaction processes from local measurements. *Fuel*, **64**, 776-781.

Vaezi, M., Passandideh-Fard, M., Moghiman, M. and Charmchi, M. (2011). Gasification of heavy fuel oils: A thermochemical equilibrium approach. *Fuel*, **90**(2), 878-885.

Versteeg, H. and Malalasekara, W. (2007). An Introduction to Computational Fluid Dynamics: The Finite Volume Method (2nd Edition), *Prentice Hall*.

Vicente, W., Ochoa, S., Aguillon, J. and Barrios, E. (2003). An Eulerian model for the simulation of an entrained flow coal gasifier. *Applied Thermal Engineering*, **23**, 1993-2008.

Wang, X.H., Zhao, D.Q., He, L.B., Jiang, L.Q., He, Q. and Chen, Y. (2007). Modeling of a coal-fired slagging combustor: Development of a slag submodel. *Combustion and Flame*, **149**, 249-260.

Watanabe, H., Otaka, M., Hara, S., Ashizawa, M., Kidoguchi, K. and Inumaru, J. (2002). Modeling and Simulation for Extra Heavy Oil Gasification on Entrained Flow Gasifier. *Proceedings of the 2002 International Joint Power Generation Conference*, 667-674.

Watanabe, H. and Otaka, M. (2006). Numerical simulation of coal gasification in entrained flow coal gasifier. *Fuel*, **85**, 1935-1943.

Wen, C.Y. and Chaung, T.Z. (1979). Entrainment Coal Gasification Modeling. *Industrial & Engineering Chemistry Process Design and Development*, **18**(4), 684-695.

Westbrook, C.K. and Dryer, F.L. (1981). Chemical Kinetics and Modeling of Combustion Processes. *Eighteenth Symposium (International) on Combustion - The Combustion Institute*, 749-767.

Wu, Y., Smith, P.J., Zhang, J., Thornock, J.N. and Yue, G. (2010). Effects of Turbulent Mixing and Controlling Mechanisms in an Entrained Flow Coal Gasifier. *Energy & Fuels*, **24**(2), 1170-1175.